Constructing Continuous Strain and Stress Fields from Spatially Discrete Displacement Measurements in Soft Materials

by

Wanru Liu

A thesis submitted in partial fulfillment of the requirements for the degree of

Master of Science

Department of Mechanical Engineering
University of Alberta

Abstract

Recent studies show that particle tracking together with moving least-square (MLS) method is capable to interpolate displacement field and to determine strain and stress fields from discrete displacement measurements in soft materials. The goal of this study is to evaluate of the numerical accuracy of MLS in determining the displacement, strain and stress fields in soft materials. Using an indentation example as the benchmark, we extracted the discrete displacements data from a finite element model and used it as the input to MLS. We assessed the accuracy of MLS by comparing displacement, strain and stress fields from MLS with the corresponding results from finite element analysis (FEA). For the indentation model, we also finished a parametric study and had some understanding towards how the parameters affect the accuracy of MLS. Based on the guideline about the effect of parameters, we applied the MLS method to two other cases with stress concentration: a plate with a circular cavity subjected to large uni-axial stretch and a plane stress crack under large Mode-I loading. The results demonstrated the capability of MLS to measure large deformation and stress concentration within soft materials.

Acknowledgments

I wish to express my sincere thanks to my supervisor, Dr. Rong Long, for providing me with the leadership, advice and funding for the research. When I need guide for a question, you always give me fast and correct feedback, which make me optimistic to the research.

I am also grateful to my co-supervisor, Dr. Tian Tang. Thank you for your tutelag, patience and high-standard. Your instructions about academic writing is so important to me that I could not finish the thesis without your help.

I also place on record, my sense of gratitude to the other graduate students in my office including Cuiying Jian, Luxia Yu, Bingjie Wu and Tamran Lengyel. I also want to thank my friends like Wuhua Zhang, Shuai Zhou, Xu Zhang and Bang Liu. Thank you for the help and encouragement. It is a memorable experience in my life!

Finally, to my dear parents, thank you very much for the support. I love you!

Table of Contents

List of Tables

List of Figures

List of Symbols

Δ	Difference in optical path
C	Stress-optic coefficient
H	The thickness of material sample
$\tilde{\lambda}$	The wavelength
σ_1	Principal stress in the first direction
σ_2	Principal stress in the second direction
ε_{33}	Normal strain in X_3 direction
μ	Shear modulus
E	Young's modulus
P	Pitch of grating
ϕ	Cross-correlation function
$f(\mathbf{X})$	Grayscale light intensity of a reference image
$\mathbf{u}(\mathbf{X})$	Displacement field in the undeformed configuration
$g(\mathbf{X}+\mathbf{u})$	Grayscale light intensity of the image after deformation
Ω	Domain in Fig. 2.1Schematic diagram to demonstrate the weight of data points. In d
A	Interpolation point in Fig. 2.1Schematic diagram to demonstrate the weight of data p
$v(\mathbf{X})$	Unknown function value of interpolation point
$\mathbf{X}$	Position vector in undeformed configuration
B_I	Data points
n	Number of data points
$\mathbf{b}_I$	Cartesian coordinates of data points
w_I	Exact function value of data points
$\tilde{v}(\mathbf{x})$	Interpolated function value

$\mathbf{P}^T(\mathbf{x})$	Interpolation basis
$\mathbf{a}(\mathbf{X})$	Position-dependent coefficients
L	Weighted least square error function
$f(\mathbf{X} - \mathbf{b}_I)$	Weight function
Ω_b	Yellow circle in Fig. 2.1Schematic diagram to demonstrate the weight of data points
$\mathbf{A}(\mathbf{X})$, $\mathbf{B}(\mathbf{X})$, $\mathbf{w}$	Parts of solution of $\mathbf{a}(\mathbf{X})$ in Eq. 2.6Basic principleequation.2.1.6
∇_X^2	Laplacian operator in undeformed configuration
$\mathbf{x}$	Position vector in deformed configuration
$\boldsymbol{\varepsilon}$	Infinitesimal Green strain tensor
∇_X	Nabla operator in undeformed configuration
$\boldsymbol{\sigma}$	Cauchy stress tensor
λ	Lame's constant
ε_b	Bulk strain
δ_{ij}	Kronecker delta
v	Poission's ratio
p	Hydrostatic pressure
$\mathbf{E}$	True strain tensor
$\mathbf{V}$	Left stretch tensor
$\mathbf{B}$	Left Cauchy Green deformation tensor
$\mathbf{F}$	Deformation gradient tensor
$\mathbf{I}$	Unit tensor
W	Strain energy density function
I_1	First invariant of the left Cauchy Green deformation tensor
J	Jacobian of the deformation gradient
β	Material constant which equals to $\frac{v}{1-2v}$
$\mathbf{S}$	First Piola-Kirchhoff stress tensor
$\tilde{p}$	Hydrostatic pressure in infinitesimal deformation
r_c	Cut-off radius
d	Distance between interpolation point and data points
m	Length of interpolation basis

r, θ, z	Axis of cylindrical coordinates
R	Radius of the indenter
h	Thickness of the gel layer
w	Width of the gel layer
δ	Indentation depth
r_1	Radius of the circular hole
l_1	Length of the plate under tension
h_1	Height of the plate under tension
u_1	A horizontal displacement
$q/2$	Length of the edge crack
l_2	Length of the plate of the crack model
h_2	Height of the plate of the crack model
u_2	A vertical displacement
μ^*	Normalized shear modulus
C_1	Material constant which is equal to $\frac{\mu}{2}$
${C_1}^*$	Normalized material constant C_1
$\mathbf{e}_r$	Basis vector for the cylindrical coordinates
$\mathbf{e}_z$	Basis vector for the cylindrical coordinates
η_i	Relative error between the results from MLS and FEA
η_{ave}	The average of relative errors
$\tilde{\eta}$	Median of relative errors
γ	Normalized nearest neighbour distance
N	Total number of grid points
S	Area of zone of interest

List of Abbreviations

2D	Two-dimensional
3D	Three-dimensional
CCD	Charged-coupled device
DIC	Digital image correlation
DVC	Digital volume correlation
FEA	Finite element analysis
LSCM	Laser scanning confocal microscope
MLS	Moving least-square
PIV	Particle image velocity
SEM	Scanning electro microscopy
STM	Scanning tunnelling microscopy
X-ray CT	X-ray computed tomography

Chapter 1

Introduction

1.1 Photomechanics

Experimental measurement of displacement, strain and stress is an essential step towards understanding the mechanical behaviors of various materials, especially for materials under complex loading conditions. There exist some traditional tools such as strain gauges which can provide very accurate measurement at discrete points of a sample. However, strain gauges still have limitations. First, a strain gage can only measure normal strain component along its direction. If multiple strain components need to be measured, we should use a rosette with three strain gages along different directions. Second, a strain gage can only give local measurement. Once the measured objective is a spatially varying strain field, multiple strain gages are required. Third, when we are using a strain gage, it needs to be attached to the surface of a sample. To avoid disturbing the deformation of the sample, the strain gage has to be relatively small and thin as compared to the sample. This makes it difficult to the application of measuring small-scale (millimeter size) samples. Therefore, researchers have been devoted to developing efficient non-contact techniques capable of full-field measurements of material deformation. Photomechanics emerged as a class of techniques that utilizes optical methods to achieve this goal. After several decades of development, it has grown into two categories: interferometric and non-interferometric techniques [1]. Next we will provide brief introduction of several examples for both techniques. A complete review of photomechanics can be found in [2] and [3].

Examples of the interferometric approaches include photoelasticity and moire method. Most measurement results are shown in fringe patterns that originate from interference of light or simple geometric patterns. The interferometric method can provide a direct visualization of strain or stress fields in a non-contact manner. It has been widely applied in optical fiber pressure sensor [4], the measurement of refractive index [5], etc.

For non-interferometric techniques, representative methods include grid methods [6], synchrotron radiation computed tomography [7] and digital image correlation (DIC). Among these methods, the digital image correlation method is especially relevant to this thesis. Unlike generating fringe patterns on the sample, it focuses on the digital images of the sample before and after mechanical deformation. These images record gray-scale light intensity information pixel by pixel across the imaging window on the specimen surface. By comparing the light intensity pattern of two images before and after deformation, locations of the pixel corresponding to the same material point in the specimen before and after deformation can be determined, and so is displacement of the pixel. This method can help generate a two-dimensional displacement field on the surface of the sample. The DIC method was further extended to three dimension (measurement of the out of plane displacement component), which is known as digital volume correlation (DVC). DVC is capable of full 3D measurement and we are going to discuss it in details later.

To motivate the work in this thesis, a number of representative optical methods for measuring deformation and stress fields are introduced in further details below.

1.1.1 Interferometric techniques

Photoelasticity [8][9][10], based on the optical property of birefringence, is an experimental approach to conduct the stress measurement inside a material. Birefringence refers to the phenomenon that when a ray of light passes through a birefringent material, it will split into two rays experiencing different refractive indices. Some materials such as optical fibers [11] and ordinary cellophane (a kind of plastics) [12] exhibit birefringence effect when they are subjected to mechanical stress. Therefore there is a possibility to relate birefringence and stress.

The stress-induced birefringence is the underlying mechanism for conducting photoelasticity experiments. First, a ray of polarized light was applied to the surface of a thin sample which is loaded in plane stress state. Then the light will split into two rays along the two principal stress directions. Since the rays of lights after split experience different refractive indices, they possess different propagation speed inside the sample, leading to a difference in optical path Δ. The magnitude of Δ can be determined using the stress-optic law [13].

$$\Delta = C\frac{2\pi H}{\tilde{\lambda}}(\sigma_1 - \sigma_2) \tag{1.1}$$

where C is the stress-optic coefficient (material constant), H is the thickness of material sample, $\tilde{\lambda}$ is the wavelength, σ_1 and σ_2 are the two principal stresses. The difference in optical path Δ leads to optical interference of the two splitted light waves and then fringe patterns known as isochromatics is formed. The fringe patterns can be named by its order which is equal to $\dfrac{\Delta}{2\pi}$. Isochromatics are the contour lines where the difference of the two principal stresses σ_1 and σ_2 are the same. However, isochromatics alone is insufficient to determine the values of both principal stresses σ_1 and σ_2. Isoclinics, the lines where the points share the same direction of principal stress, is another contour required to measure the principal stresses. Isoclinics usually appear together with isochromatics. It can be separated from isochromatics by several methods including center fringe method, the phase-shift method, etc [14].

Once directions of the two principle stresses (σ_1, σ_2) and the difference between them are obtained, the principal stresses can be computed using elasticity theories [15]. However, the quality of isoclinics was not very good since it is hard to obtain isoclinics without the interference from isochromatics [14]. In 1990, Brown and Sullivan [16] proposed a polarization-stepping method to record isoclinics using polarized light. To reduce the noise from isochromatics, they minimized the applied load to make sure the orders of resulted fringes are less than or equal to 0.5 [9]. In 1999, Petrucci [14] improved Brown's and Sullivan's experiment [16] by using white light instead of polarized light and succeeded in decreasing the interaction from isochromatics and obtaining accurate measurements of isoclinics [9].

Besides isoclinics, isopachics is another quantity that was used to measure principal stresses together with isochromatics. Isopachics is the contour lines where the points have the same out-of-plane normal strain ε_{33} . According to Hooke's law, ε_{33} is proportional to the sum of two principal stresses in plane stress state [17],

$$\varepsilon_{33} = -\frac{\mu}{E}(\sigma_1 + \sigma_2) \tag{1.2}$$

where μ is the shear modulus and E is the Young's modulus. The application of isopachics also suffers from a limitation: it requires two samples with the same mechanical properties and under the same stress state, one with birefringence and one without, so that both the isochromatics (or $\sigma_1 - \sigma_2$) and isopachis (or ε_{33}) can be measured [17]. The sample with no birefringence is required to measure isopachics without being affected by the isochromatics. There is another technique using holography [18] to obtain isopachics and isochromatics at one time by double exposure. However, the fringes obtained from holography are very complicated to analyze [17].

Moire method is another optical technique using interference to measure deformation. The term moire is derived from French, referring to the rippled pattern formed when two pieces of silk fabric covered each other. In experimental mechanics, moire pattern refers to the fringes formed by superimposing two gratings together. Moire pattern can be formed in two ways: geometric interference and moire interferometry. Their underlying principles are different. We first introduce the basic principle of geometric interference. Line grating, consisting of parallel equidistant dark lines and bright lines, is one of the most common gratings to conduct geometric interference. The reference grating shown in Fig. 1.1Schematic of Moire pattern formed by geometric interference of line gratings.figure.caption.8 represents the typical structure of a line grating. An important property of grating is the pitch P, which is the distance between neighbouring dark lines. The pitch P characterizes the density of lines. When two identical line gratings are overlaid completely, they appear as a single grating. However, if one grating referred to as the specimen grating is attached to a sample, the specimen grating would deform together with the sample when it is subjected mechanical loading (e.g. under compression in Fig. 1.1Schematic of Moire pattern formed by geometric interference of line gratings.figure.caption.8). As a result, the pitch of the specimen grating changes, it no longer coincides with the other grating named as the reference grating which is not attached to the sample and thus is undeformed. The dark lines of specimen grating will cover the bright lines of reference grating and then form dark fringes. The superposition of bright lines from the two gratings will become bright fringes. The bright and dark fringes formed in this way are moire pattern. The position and spacing of moire pattern reflect the deformation of the sample, so the displacement and strain of the sample can be determined by measuring the moire pattern.

Geometric interference is often applied to gratings with low densities to generate moire pattern which can be seen by naked eyes [19]. However, if grating of higher density is utilized, the mechanism is different since diffraction of light becomes dominant, rather than the simple geometric interferometry. Therefore, coherent light is needed to observe moire pattern [19]. This technique is known as

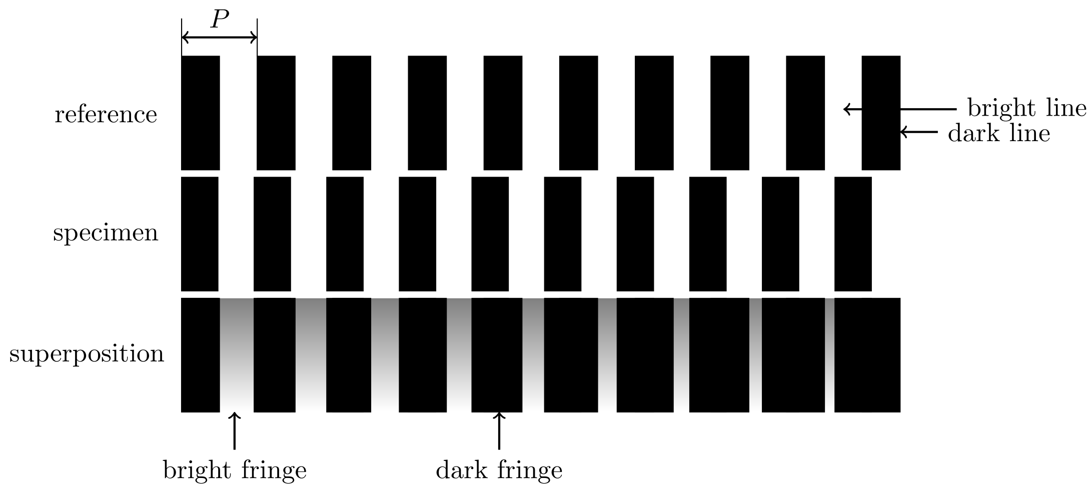

Fig. 1.1. Schematic of Moire pattern formed by geometric interference of line gratings.

the moire interferometry. Moire interferometry has been utilized in a lot of fields like the measurements of refractive index and refractive index gradient [5], determination of residual stress [20][21] and dental materials [22]. The details of moire interferometry will not be presented here but can be found in the paper of Nicoletto et al.[20] as well as Post and Baracat [23].

1.1.2 Non-interferometric techniques

As is mentioned in Section 1.1Photomechanicssection.1.1, DIC is a widely used non-interferometric method and is closely related to the work in this thesis. Here we will briefly review the operating mechanism of the DIC method.

DIC was first developed by researchers at the University of South Carolina in 1980s [1][24][25]. Based on digital image analysis and numerical computation, it is typically used to measure displacement in solid materials undergoing mechanical deformation. The basic principle is to match the pixels representing the same material point between two images before and after deformation. The matching can be achieved by maximizing a cross-correlation function defined in the following:

$$\phi = \int\int f(\mathbf{X})g(\mathbf{X}+\mathbf{u})d\mathbf{X} \tag{1.3}$$

where $f(\mathbf{X})$ is the grayscale light intensity of a reference image, $\mathbf{u}(\mathbf{X})$ is the in-plane displacement field and $g(\mathbf{X}+\mathbf{u})$ represents the grayscale light intensity of the image after deformation. To conduct displacement measurement using DIC, first the specimen needs to be prepared with a carrier of deformation information, which can be a speckle pattern on the surface. The speckle pattern comes either from the naturally occurring properties such as the texture of the specimen material, or artificially introduced, i.e. random paint pattern. There is a similar methodology which has been applied in experimental fluid mechanics. It is known as particle image velocity (PIV). It is utilized to measure the velocity of fluid by tracing the particles seeded within the fluid [1]. Details concerning this method can be found in [26][27][28].

DIC has several advantages that makes it appealing. First, a white light is enough for illumination in DIC, rather than a laser source for moire interferometry [1]. Second, due to the use of advanced optical instruments such as laser scanning confocal microscope (LSCM) [29][30], scanning tunnelling microscope (STM)[31] and scanning electron microscopy (SEM) [32][33], the sensitivity and accuracy of DIC have been improved over recent years [1]. Besides, there are various algorithms such as coarse-fine search algorithm [34] and spatial-gradient-based algorithm [35] developed to improve the accuracy.

In 1993, Luo et al. [36] first proposed three-dimensional digital image correlation (3DDIC), a combination of the DIC technique and a stereo pair of CCD cameras, to achieve full-field 3D surface measurement. From that, there is a large growth in the development of 3DDIC and it has a wide range of applications in aerospace [37], biomechanics [38] and experimental solid mechanics [39]. However, 3DDIC is still a surface based method restricted to visible surfaces of the specimen. In certain applications, it is important to develop a technique which can achieve three dimensional displacement measurements in bulk materials. Motivated by this goal, the first generation of digital volume correlation (DVC) was developed in 1999 as a solution to trace the displacement and strain fields inside trabecular bone tissue [40]. While DIC is to track the displacements of areal pixels which are small regions of speckle or material texture, DVC extends areal pixel to volumetric voxel. The implementation of DVC relies on another technology: high-resolution X-ray computed tomography, or X-ray CT. X-ray CT uses computer processed X-ray to take tomographic images of specific areas of a scanned specimen. It allows the researchers to observe the inside of the specimen without cutting it. X-ray CT also broadens the measurement scale of DVC because of its high resolution, which enables to image sample owning complex structure [41].

Subsequent refinements towards DVC relies on the improvements of correlation algorithms [41]. Different from tracking displacement like DIC, rotational degree of freedom of the voxel element was introduced by Smith et al. [42], which decreases the error in the consideration of rigid body rotation. Franck et al. [29] accounted for the stretch of the voxel element in their correlation algorithms. The improvements did help enhance the accuracy of DVC, but it also increases the complexity of the algorithms and the time required for computation.

1.2 Application to soft material measurement

Soft material has become interest of many scientists and engineers due to its attractive features like bio-compatibility, large deformability and stimuli-responsiveness. The application of soft material covers a lot of fields including soft robotics [43], soft actuator [44], tissue engineering [45] and biomedical implants [46]. Probing the mechanical property of soft material is very active now since it is closely related to the deep understanding and technical application of soft materials.

For traditional engineering materials (e.g. metal and ceramics), their deformation can be described by the linear elasticity. However, linear elasticity theory cannot be applied to soft materials since it can undergo large nonlinear deformation. Therefore, it motivates a lot of researches trying to propose more complicated models accounting for the geometrical and material nonlinearity of soft materials [47]. The question is that development of these theoretical models relies on the advancement of fundamental understanding of soft material mechanics which requires significant experimental data. This is especially true for material samples with complex geometry and loading conditions. Typical cases include the measurement of cell traction on the substrate [48][49][50] and the fracture of soft materials [51].

Since it is not possible to paint speckle patterns in the interior of a specimen in the experiments, DVC usually employs specimen which has naturally occurring material texture [52]. For soft elastomers and gels, however, one can introduce artificial volumetric patterns by embedding fluorescent particles in the samples during the synthesis process. For the instrument of imaging, since most soft materials are transparent, images can be taken using a fluorescent microscope instead of X-ray CT. In 2007, Franck et al. [29] developed a method to measure the nonlinear deformation of soft materials based on DVC. The innovations of their method are in the following aspects. One is that for the first time, they induced artificial volumetric patterns by incorporating fluorescent particles in soft materials which typically do not possess natural volumetric patterns. Secondly, the voxel was not treated as a rigid body; the deformation of each voxel, potentially caused by large bulk deformation, was taken into account in the correlation algorithm. Despite its originality, Franck et al.'s [29] method still has several limitations. First, rotations and shear deformation of the voxel elements were neglected in the correlation algorithm. Only stretching deformation for the voxel elements were considered. This assumption may be satisfied in general and may reduce the accuracy of measurements. Second, to improve the spatial resolution of the measured field, the size of the voxel elements needs to be sufficiently small. However, the size of voxels was limited by the spacing of the fluorescence particles, i.e., a voxel should at least include two to three fluorescence particles to show a unique volumetric pattern. Third, to obtain the strain field, or the gradient of the displacement field, complicated algorithms are needed to to conduct smoothing or filtering procedures. Otherwise, the measured strain fields may be non-smooth, which limits the application of this method for problems involving non-uniform deformation especially those with severe stress concentration.

1.3 Particle tracking method for full-field measurement in soft materials

Recently Hall et al. [53] developed a new method to map three-dimensional strain and stress fields within a soft hydrogel. Their method is based on tracking the displacement of fluorescent beads embedded in the hydrogels. Unlike the DVC method where voxel elements containing several fluorescent particles are tracked, here individual particles are tracked which is expected to lead to a higher spatial resolution for the measured field. However, the difficulty lies in how to interpolate the displacements measured at a set of randomly distributed particles and obtain a continuous displacement field and its gradient. This issue was nicely addressed by a numerical interpolation technique known as moving least square (MLS). In 1994, a element-free galerkin method was proposed by Belytschko et al. [54] as an alternative for finite element method. A core component of the element-free galerkin method was based on the moving least-square (MLS) method, which provides shape functions for interpolating the displacement field from randomly distributed nodes. Originally the MLS method was developed in computer graphics, e.g., for the regeneration of a surface based on the coordinates of discrete point on the surface [55][56]. The MLS method was also used for computing strain from displacements at some arbitrary points [57]. The advantages of this technique include: 1), it is not restricted to the measurement of linear elastic deformation or small deformation, but can be extended to nonlinearities of soft material; 2), the MLS can generate continuous derivatives of any order and then guarantee the smoothness of strain fields. Therefore, particle tracking together with MLS interpolation method is expected to greatly facilitate the experimental study of large and nonlinear deformation within soft materials.

1.4 Objectives of this project

The focus of this thesis is to assess the numerical accuracy of MLS in determining the continuous displacement, strain and stress fields from discrete displacement measurements in soft materials. First, we use FEA to simulate some representative cases of large deformation in soft materials. Then we will extract the displacement of a set of randomly selected nodes and use it as the input data for MLS interpolation. After we obtain the continuous displacement, strain and stress fields from MLS interpolation, we compare them with the corresponding results from FEA to assess the accuracy. In addition, the implements of MLS method also require us to specify a number of parameters which will be detailed in Chapter 2Introduction to the moving least-square methodchapter.2. We considered the effects of parameters on the accuracy of MLS method and the optimized choice of parameters. Furthermore, we extended the MLS-based data processing method in Hall et al. [53], so that it is capable of solve large deformation problems with geometrical nonlinearity. We also studied the potential of applying the particle tracking and MLS method for loading scenarios with severe stress concentration.

The thesis is arranged as follows. The moving least-square method is illustrated in details in Chapter 2Introduction to the moving least-square methodchapter.2. In Chapter 3Models and methodchapter.3, the models are specifically introduced and the criterion for evaluating the accuracy of MLS is proposed. The results for the models are given in Chapter 4Results for the indentation example and parametric studychapter.4 and 5Application cases with stress concentrationchapter.5. Chapter 6Conclusions and future workchapter.6 is concerning the conclusions and future work.

Chapter 2

Introduction to the moving least-square method

2.1 Basic principle

The moving least-square (MLS) method is an interpolation method to construct a function through a set of unorganized data points. The detailed process is reviewed in this section. Suppose in a domain Ω, there is a point A whose function value $v(\mathbf{X})$ is required to be determined (see Fig. 2.1Schematic diagram to demonstrate the weight of data points. In domain Ω (the purple square), A is a point whose displacement we are interested in. B_1, B_2 and B_3 are the data points near A. The yellow circle Ω_b centered at X differentiates the weight of data points. Only data points inside Ω_b contribute to the interpolation.figure.caption.9). Here $\mathbf{X}$ denotes the position vector of A, i.e., $\mathbf{X}^T = [X_1, X_2, X_3]$. There are also n data points $B_I(I = 1, 2, 3, ..., n)$ randomly distributed in Ω (the data points are the fluorescent beads with experimentally measured displacements mentioned in Section 1.3Particle tracking method for full-field measurement in soft materialssection.1.3) . Each has a position vector of $\mathbf{b}_I(I = 1, 2, 3, ..., n)$. Besides, their exact function values are given by $w_I \equiv v(\mathbf{b}_I)(I = 1, 2, 3, ..., n)$. The interpolated function value $\tilde{v}(\mathbf{X})$ can be found by introducing a interpolation basis $\mathbf{P}^T(\mathbf{X})$ and the corresponding coefficients $\mathbf{a}(\mathbf{X})$ as follows [54]:

$$\tilde{v}(\mathbf{X}) = \mathbf{P}^T(\mathbf{X})\mathbf{a}(\mathbf{X}) \tag{2.1}$$

where $\mathbf{P}^T(\mathbf{X})$ is composed of polynomials and $\mathbf{a}(\mathbf{X}) = [a_0(\mathbf{X}), a_1(\mathbf{X}), a_2(\mathbf{X}), ...]^T$ are the unknown coefficients. For example, in a three dimensional domain, if a linear basis is used, $\mathbf{P}^T(\mathbf{X}) = [1, X_1, X_2, X_3]$ and $\tilde{v}(\mathbf{X}) = a_0(\mathbf{X}) + a_1(\mathbf{X})X_1 + a_2(\mathbf{X})X_2 + a_3(\mathbf{X})X_3$. It should be noted that the coefficient $\mathbf{a}(\mathbf{X})$ is dependent on the position of the interpolation point (e.g. point A in Fig. 2.1Schematic diagram to demonstrate the weight of data points. In domain Ω (the purple square), A is a point whose displacement we are interested in. B_1, B_2 and B_3 are the data points near A. The yellow circle Ω_b centered at X differentiates the weight of data points. Only data points inside Ω_b contribute to the interpolation.figure.caption.9), not a constant for traditional polynomial interpolation. Therefore, the interpolation function $\tilde{v}(\mathbf{X})$ is able to accommodate complicated function that does not resemble polynomial functions.

The position-dependent coefficients $\mathbf{a}(\mathbf{X})$ can be determined by minimizing a weighted least-square error function L which is defined as

$$L = \sum_{I=1}^{n} f(\mathbf{X} - \mathbf{b}_I)[\mathbf{P}^T(\mathbf{b}_I)\mathbf{a}(\mathbf{X}) - w_I]^2 \tag{2.2}$$

where $f(\mathbf{X} - \mathbf{b}_I)$ is a weight function that decays as the distance between the data point at $\mathbf{b}_I$ and the interpolation point at $\mathbf{X}$, or $|\mathbf{X} - \mathbf{b}_I|$, increases. This decaying characteristics of the weight function $f(\mathbf{X} - \mathbf{b}_I)$ is consistent with the position-dependent attribute of $\mathbf{a}(\mathbf{X})$. That is, data points closer to point A contribute more to the weighted least-square error function L. Typically to simplify the calculation, a cut-off radius r_c is introduced to exclude the data points beyond r_c; in other words, the weight function is zero for those data points outside the cut-off radius r_c. Fig. 2.1Schematic diagram to demonstrate the weight of data points. In do-

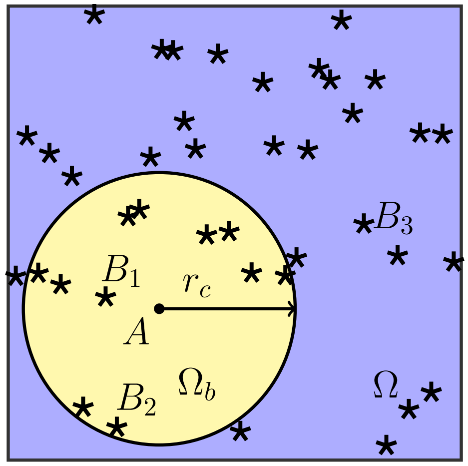

Fig. 2.1. Schematic diagram to demonstrate the weight of data points. In domain Ω (the purple square), A is a point whose displacement we are interested in. B_1, B_2 and B_3 are the data points near A. The yellow circle Ω_b centered at X differentiates the weight of data points. Only data points inside Ω_b contribute to the interpolation.

main Ω (the purple square), A is a point whose displacement we are interested in. B_1, B_2 and B_3 are the data points near A. The yellow circle Ω_b centered at X differentiates the weight of data points. Only data points inside Ω_b contribute to the interpolation.figure.caption.9 can help us better understand how weight function $f(\mathbf{X} - \mathbf{b}_I)$ works. B_1, B_2 and B_3 are representative data points around the interpolation point A. A circular domain Ω_b centered at A with the cut-off radius r_c defines a region where only data points inside it have non-zero weight and can contribute to the weighted least-square error function L. Since B_1 and B_2 are inside Ω_b, their contribution is not zero. The weight of B_2 is smaller than that of B_1 because B_1 is closer to A. However, point B_3 is outside the domain Ω_b, thus its weight is zero.

To find the minimum of L, we set the first-order derivative of L with respect to $\mathbf{a}(\mathbf{X})$ to be zero, i.e.,

$$2\sum_{I=1}^{n} f(\mathbf{X} - \mathbf{b}_I)[\mathbf{P}^T(\mathbf{b}_I)\mathbf{a}(\mathbf{X}) - w_I]\mathbf{P}(\mathbf{b}_I) = 0 \tag{2.3}$$

Eq. 2.3Basic principleequation.2.1.3 is an linear equation for $\mathbf{a}(\mathbf{X})$ and the solution is listed below [54]:

$$\mathbf{a}(\mathbf{X}) = \mathbf{A}^{-1}(\mathbf{X})\mathbf{B}(\mathbf{X})\mathbf{w} \tag{2.4}$$

where

$$\mathbf{A}(\mathbf{X}) = \sum_{I=1}^{n} f(\mathbf{X} - \mathbf{b}_I)\mathbf{P}(\mathbf{b}_I)\mathbf{P}^T(\mathbf{b}_I) \tag{2.5a}$$

$$\mathbf{B}(\mathbf{X}) = [f(\mathbf{X} - \mathbf{b}_1)\mathbf{P}(\mathbf{b}_1), ..., f(\mathbf{X} - \mathbf{b}_n)\mathbf{P}(\mathbf{b}_n)] \tag{2.5b}$$

$$\mathbf{w}^T = [w_1, w_2, ..., w_n] \tag{2.5c}$$

where $f(\mathbf{X} - \mathbf{b}_I)$ is the weight function, $\mathbf{b}_I(I = 1, 2, 3, ..., n)$ is the position vector of data points and $w_I(I = 1, 2, 3, ..., n)$ is the exact function value of data points. Therefore, the interpolated function value $\tilde{v}(\mathbf{X})$ can be expressed as

$$\tilde{v}(\mathbf{X}) = \mathbf{P}^T(\mathbf{X})\mathbf{a}(\mathbf{X}) = \mathbf{P}^T(\mathbf{X})\mathbf{A}^{-1}(\mathbf{X})\mathbf{B}(\mathbf{X})\mathbf{w} \tag{2.6}$$

Due to the need of calculating strain and stress fields (detailed in the next section), we have to get the first-order derivative and Laplacian of $\tilde{v}(\mathbf{X})$:

$$\frac{\partial \tilde{v}}{\partial X_j} = \left[\frac{\partial \mathbf{P}^T}{\partial X_j}\mathbf{A}^{-1}\mathbf{B} - \mathbf{P}^T\mathbf{A}^{-1}\frac{\partial \mathbf{A}^T}{\partial X_j}\mathbf{A}^{-1}\mathbf{B} + \mathbf{P}^T\mathbf{A}^{-1}\frac{\partial \mathbf{B}}{\partial X_j}\right]\mathbf{w} \tag{2.7}$$

$$\begin{aligned}\nabla_X^2 \tilde{v} = [&(\nabla_X^2 \mathbf{P}^T)\mathbf{A}^{-1}\mathbf{B} - \mathbf{P}^T\mathbf{A}^{-1}(\nabla_X^2 \mathbf{A})\mathbf{A}^{-1}\mathbf{B} + \mathbf{P}^T\mathbf{A}^{-1}(\nabla_X^2 \mathbf{B}) \\ &+ \sum_{j=1}^{3} 2\frac{\partial \mathbf{P}^T}{\partial X_j}(-\mathbf{A}^{-1})\frac{\partial \mathbf{A}}{\partial X_j}\mathbf{B} + \mathbf{A}^{-1}\frac{\partial \mathbf{B}}{\partial X_j)} \\ &+ \sum_{j=1}^{3} 2\mathbf{P}^T(\mathbf{A}^{-1}\frac{\partial \mathbf{A}}{\partial X_j}\mathbf{A}^{-1}\frac{\partial \mathbf{A}}{\partial X_j}\mathbf{A}^{-1}\mathbf{B} \\ &- \mathbf{A}^{-1}\frac{\partial \mathbf{A}}{\partial X_j}\mathbf{A}^{-1}\frac{\partial \mathbf{B}}{\partial X_j})]\mathbf{w}\end{aligned} \tag{2.8}$$

where the subscript j could be 1, 2 or 3, representing Cartesian coordinates X_1, X_2 and X_3, respectively.

In all, MLS is an interpolation method allowing the coefficients $a(\mathbf{X})$ to be position-dependent. Without the position-dependent coefficients $a(\mathbf{X})$, the derivative of the interpolation function may be very inaccurate if low order polynomial basis functions are used (e.g. linear polynomial basis). The position-dependent coefficient together with the weight function in the weighted least-square error L ensure that MLS can build an interpolation function continuous up to any order. In this way, for any arbitrary point in Ω, we can calculate its interpolated function value $\tilde{v}(\mathbf{X})$ from the given data points. Repeating this process for every point in Ω, a continuous field can be established.

2.2 Displacement, strain and stress fields

The displacement of a material point in a solid is defined as:

$$\mathbf{u}(\mathbf{X}) = \mathbf{x} - \mathbf{X} \tag{2.9}$$

where **X** and **x** are the position vectors of the material point in undeformed and deformed configurations and **u** is the displacement vector, i.e. $\mathbf{u}^T = [u_1, u_2, u_3]$. If the MLS method is applied to each of the three displacement components, an interpolated displacement field can be constructed from the given displacement measurements at a set of data points.

For infinitesimal deformation, the strain field can be calculated from displacement field using the definition of the Green strain tensor in linear elasticity.

$$\boldsymbol{\varepsilon} = \frac{\nabla_X \mathbf{u} + (\nabla_X \mathbf{u})^T}{2} \tag{2.10a}$$

$$\text{or} \quad \varepsilon_{ij} = \frac{1}{2}(\frac{\partial u_i}{\partial X_j} + \frac{\partial u_j}{\partial X_i}) \tag{2.10b}$$

where the subscripts i and j can be 1 ,2 or 3. In this case, once the displacement field is determined by MLS, the components of Green strain tensor can be computed using Eq. 2.7Basic principleequation.2.1.7 and Eq. 2.10Displacement, strain and stress fieldsequation.2.2.10b.

In linear elasticity, for isotropic materials the stress tensor can be determined from the strain tensor using the Hooke's law:

$$\boldsymbol{\sigma} = \lambda \varepsilon_b \mathbf{I} + 2\mu \boldsymbol{\varepsilon} \tag{2.11a}$$

$$\text{or} \quad \sigma_{ij} = \lambda \varepsilon_b \delta_{ij} + 2\mu \varepsilon_{ij} \tag{2.11b}$$

where λ is the Lame's constant, $\varepsilon_b = \varepsilon_{11} + \varepsilon_{22} + \varepsilon_{33}$ is the bulk strain, $\mathbf{I}$ is the unit tensor, μ is the shear modulus and $\boldsymbol{\varepsilon}$ is the Green strain tensor. The Lames's constant λ can be calculated from

$$\lambda = \frac{Ev}{(1+v)(1-2v)} \tag{2.12}$$

where E is the Young's modulus and v is the Poission's ratio. A difficulty arises if the material is nearly incompressible which is the case for most soft elastomers and gels. In this case, the Poission's ratio is close to $\frac{1}{2}$. As a result, the value of λ approaches infinity as shown in Eq. 2.12Displacement, strain and stress fieldsequation.2.2.12, and the bulk strain ε_b approaches zero. This makes the first term on the right hand side of Eq. 2.11Displacement, strain and stress fieldsequation.2.2.11b indeterminate. Hall et al. [53] proposed a solution by replacing $\lambda \varepsilon_b$ in Eq. 2.11Displacement, strain and stress fieldsequation.2.2.11b with $-\tilde{p}$ where $\tilde{p}$ is referred to an unknown hydrostatic pressure and is a field variable. Then the stress component becomes

$$\sigma_{ij} = -\tilde{p}\delta_{ij} + 2\mu \varepsilon_{ij} \tag{2.13}$$

where δ_{ij} is Kronecker delta. Since σ_{ij} has to satisfy the equilibrium equation which is in the following form if body forces are neglected:

$$\sum_{j=1}^{3} \frac{\partial \sigma_{ij}}{\partial x_j} = 0 \tag{2.14}$$

where x_j is in deformed configuration. $\tilde{p}$ can be determined by substituting Eq. 2.13Displacement, strain and stress fieldsequation.2.2.13 to Eq. 2.14Displacement, strain and stress fieldsequation.2.2.14, which gives us

$$\sum_{j=1}^{3} \frac{\partial \tilde{p}}{\partial x_j} \delta_{ij} = \sum_{j=1}^{3} 2\mu \frac{\partial \varepsilon_{ij}}{\partial x_j} \tag{2.15a}$$

$$\frac{\partial \tilde{p}}{\partial x_i} = 2\mu \frac{\partial \varepsilon_{ij}}{\partial x_j} \tag{2.15b}$$

It is more convenient to integrate in undeformed configuration than in deformed configuration (the reason will be presented later). In linear elasticity, the deformation is infinitesimal, and thus the undeformed and deformed configuration are in distinguishable. Therefore, $\frac{\partial \tilde{p}}{\partial x_i}$ can be replaced by $\frac{\partial \tilde{p}}{\partial X_i}$. If we recall Eq. 2.10Displacement, strain and stress fieldsequation.2.2.10b and substitute it into Eq. 2.15Displacement, strain and stress fieldsequation.2.2.15b, we obtain

$$\begin{aligned} \frac{\partial \tilde{p}}{\partial X_i} &= 2\mu \frac{\partial \varepsilon_{ij}}{\partial X_j} \\ &= \mu\left(\frac{\partial^2 u_i}{\partial X_j \partial X_j} + \frac{\partial^2 u_i}{\partial X_i X_j}\right) \\ &= \mu \nabla_X^2 u_j + \mu \frac{\partial \varepsilon_b}{\partial x_i} \end{aligned} \tag{2.16}$$

Take the integral of Eq. 2.16Displacement, strain and stress fieldsequation.2.2.16 from a reference point $\mathbf{X}_0$ to $\mathbf{X}$, we have

$$\tilde{p}(\mathbf{X}) - \tilde{p}(\mathbf{X}_0) = \mu \int_{\mathbf{X}_0}^{\mathbf{X}} (\nabla_X^2 \mathbf{u}) \cdot d\mathbf{s} + \mu[\varepsilon_b(\mathbf{X}) - \varepsilon_b(\mathbf{X}_0)]. \tag{2.17}$$

where $\nabla_X^2 \mathbf{u}$ is obtained by applying Eq. 2.8Basic principleequation.2.1.8 to the three displacement components. In order to find the unknown hydrostatic pressure field $\tilde{p}(\mathbf{X})$, one can always choose a point where one of the normal stress components (σ_{11}, σ_{22} and σ_{33}) is known at the reference point $\mathbf{X}_0$ in Eq. 2.17Displacement, strain and stress fieldsequation.2.2.17. This is because $\tilde{p}(\mathbf{X}_0)$ can be calculated from the known normal stress component at $\mathbf{X}_0$ and the strain components. Usually, the known normal stress component comes from the traction boundary conditions. For example, if $\sigma_{22}(\mathbf{X}_0) = 0$, recall Eq. 2.13Displacement, strain and stress fieldsequation.2.2.13, we can find that $\tilde{p}(\mathbf{X}_0) = 2\mu\varepsilon_{22}$. After the pressure field is obtained, stress field can then be computed using Eq. 2.13Displacement, strain and stress fieldsequation.2.2.13.

It should be noted that Hall et al. [53] are the first to propose this approach to determine hydrostatic pressure. However, their derivations are based on the assumption of infinitesimal deformation where linear elasticity applies. If the deformation is large which is typically the case for soft materials, linear elasticity theory is no longer applicable and nonlinear formulation is required. Therefore, the formulation for nonlinear deformation will be developed in the following part. For finite strain deformation, a measure of the deformation is the true strain tensor:

$$\mathbf{E} = \ln \mathbf{V} \tag{2.18}$$

where $\mathbf{E}$ is the true strain tensor and $\mathbf{V}$ is the left stretch tensor. The left stretch tensor $\mathbf{V}$ is obtained from

$$\mathbf{V} = \mathbf{B}^{\frac{1}{2}} = (\mathbf{F}\mathbf{F}^T)^{\frac{1}{2}} \tag{2.19}$$

where $\mathbf{B}$ is the left Cauchy Green deformation tensor and $\mathbf{F}$ is the deformation gradient tensor and can be calculated from

$$\mathbf{F} = \nabla_X \mathbf{u} + \mathbf{I} \tag{2.20a}$$

$$\text{or} \quad F_{ij} = \delta_{ij} + \frac{\partial u_i}{\partial X_j} \tag{2.20b}$$

So

$$B_{ij} = F_{ik}F_{jk} = (\delta_{ik} + \frac{\partial u_i}{\partial X_k})(\delta_{jk} + \frac{\partial u_j}{\partial X_k}) \tag{2.20c}$$

where **I** is unit tensor and δ_{ij} is Kronecker delta. $\dfrac{\partial u_i}{\partial X_j}$ can be obtained using Eq. 2.7Basic principleequation.2.1.7.

The stress-strain relations of soft elastic materials under large deformation can be described by hyperelastic material models. Neo-Hookean material, proposed by Treloar [58][59], is the simplest and one of most widely used hyperelastic material models. It is based on considering the Helmholtz free energy of a molecular network with Gaussian chain length distribution (details can be found in Bonora et al.'s book [60]). However, most soft materials undergo isochoric deformation and therefore are modelled as incompressible materials. This makes the calculation of stresses challenging. Take the incompressible neo-Hookean material as an example, and its strain energy density is

$$W = \frac{\mu}{2}(I_1 - 3) \tag{2.21}$$

where μ is the shear modulus and I_1 is the first invariant of the left Cauchy Green deformation tensor **B**. For finite deformation, there are several different stress measures such as Piola-Kirchhoff stress tensor, Second Piola-Kirchhoff stress tensor and Cauchy stress tensor. They represent stress relative to different configurations. Among them, we choose the Cauchy stress tensor which describes the true stress in the deformed configuration (relating force in deformed configuration to areas in the deformed configuration) to measure the finite stress here. The Cauchy stress for incompressible neo-Hookean material is

$$\boldsymbol{\sigma} = -p\mathbf{I} + \mu\mathbf{B} \tag{2.22}$$

where p is a Lagrange multiplier to enforce the incompressibility constraint $J = det\mathbf{F} = 1$.The term p is unknown and cannot be determined from the deformation gradient **F**. Even if the material is not exactly but close to incompressible, significant numerical errors may arise in the Cauchy stress. For example, consider the following compressible neo-Hookean material model [61][62],

$$W = \frac{\mu}{2}(I_1 - 3) + \frac{\mu}{2\beta}(J^{-2\beta} - 3) \tag{2.23}$$

where $J = det\mathbf{F}$ and β is related to the Poisson's ratio υ through $\beta = \frac{\upsilon}{1-2\upsilon}$. In this case, the Cauchy stress tensor is

$$\boldsymbol{\sigma} = -\mu J^{-2\beta-1}\mathbf{I} + \frac{\mu}{J}\mathbf{B} \tag{2.24}$$

If the material is nearly incompressible, namely that the Poisson's ratio approaches $\frac{1}{2}$, J remains close to 1 and $\beta \to \infty$. This may lead to numerical difficulties when evaluating the term $J^{-2\beta-1}$ in Eq. 2.24Displacement, strain and stress fieldsequation.2.2.24. This problem was also noted in Hall et al.[53] for linear elasticity theory where a large bulk modulus is multiplied by a small bulk strain.

To circumvent the numerical difficulty in determining stress, we first combine the Cauchy stress expression for incompressible and compressible neo-Hookean material, as listed in Eq. 2.22Displacement, strain and stress fieldsequation.2.2.22 and Eq. 2.24Displacement, strain and stress fieldsequation.2.2.24, respectively, into the following general expression:

$$\boldsymbol{\sigma} = -p\mathbf{I} + \frac{\mu}{J}\mathbf{B} \tag{2.25}$$

For the incompressible model, $J = 1$ and Eq. 2.25Displacement, strain and stress fieldsequation.2.2.25 reduces to Eq. 2.22Displacement, strain and stress fieldsequation.2.2.22. For the compressible model, the term p can be calculated using $p = \mu J^{-2\beta-1}$, but this is not practically feasible if the Poisson's ratio approaches $\frac{1}{2}$. Using Eq. 2.25Displacement, strain and stress fieldsequation.2.2.25, we can calculate the first

Piola-Kirchhoff stress tensor **S** which is

$$\mathbf{S} = J\sigma\mathbf{F}^{-T} = -Jp\mathbf{F}^{-T} + \mu\mathbf{F} \tag{2.26}$$

We assume no body forces in the material and no inertial effects. This means **S** must satisfy the equilibrium equation $\nabla_X \cdot \mathbf{S} = 0$, which, together with the Piola identity that $\nabla_X \cdot (J\mathbf{F}^{-T}) = 0$ [61], leads to an equation for the gradient of p in the undeformed configuration:

$$\nabla_X p = \frac{\mu}{J}\mathbf{F}^T(\nabla_X^2 \mathbf{u}) \tag{2.27a}$$

$$\text{Or} \qquad \frac{\partial p}{\partial X_k} = \sum_{m=1}^{3} \frac{\mu}{J}\frac{\partial^2 u_i}{\partial X_m \partial X_m} F_{ik} \tag{2.27b}$$

Integrating Eq. 2.27Displacement, strain and stress fieldsequation.2.2.27(a) from a reference point $\mathbf{X}_0$ to the interpolation point **X**, we obtain

$$p(\mathbf{X}) - p(\mathbf{X}_0) = \mu \int_{\mathbf{X}_0}^{\mathbf{X}} \frac{1}{J}(\nabla_X^2 \mathbf{u}) \cdot (\mathbf{F} d\mathbf{s}). \tag{2.28}$$

Similarly like Eq. 2.17Displacement, strain and stress fieldsequation.2.2.17, $\mathbf{X}_0$ is chosen to be a point where one of normal stresses is known. The reason why we choose to perform the integration in undeformed configuration is that we need to take another step to find positions of interpolation points in the deformed configuration. Besides, all the derivations of MLS are based on undeformed configuration. If we have to integrate in the deformed configuration, we need to modify the interpolation function Eq. 2.6Basic principleequation.2.1.6 on the deformed configuration and then we can get the corresponding first and second-order derivatives of displacement. The integral in Eq. 2.28Displacement, strain and stress fieldsequation.2.2.28 should be independent of integration path since p is uniquely defined at each point **X**. Eq. 2.28Displacement, strain and stress fieldsequation.2.2.28 provides a method to determine the hydrostatic term p for the incompressible neo-Hookean material. It is also valid for the compressible neo-Hookean material, and is useful for cases with $\beta \to \infty$ or $\upsilon \to \frac{1}{2}$. For other incompressible material models, Eq. 2.28Displacement, strain and stress fieldsequation.2.2.28 will need to be modified but the same derivation process illustrated above can be followed.

Next we are going to show how Eq. 2.28Displacement, strain and stress fieldsequation.2.2.28 reduces to the linear elastic formula presented in Hall et al. [53]. For infinitesimal deformation, the left Cauchy Green deformation tensor **B** is approximately

$$\mathbf{B} = \mathbf{F}\mathbf{F}^T = (\nabla_X \mathbf{u} + \mathbf{I})((\nabla_X \mathbf{u})^T + \mathbf{I}) \approx \nabla_X \mathbf{u} + (\nabla_X \mathbf{u})^T + \mathbf{I} \equiv 2\boldsymbol{\varepsilon} + \mathbf{I} \quad (2.29)$$

where $\boldsymbol{\varepsilon}$ is the linear strain tensor. Besides, in this case,

$$J \approx 1 - \varepsilon_b \quad (2.30)$$

where ε_b is the bulk strain. Substituting Eq. 2.29Displacement, strain and stress fieldsequation.2.2.29 and Eq. 2.30Displacement, strain and stress fieldsequation.2.2.30 into Eq. 2.25Displacement, strain and stress fieldsequation.2.2.25 and keeping only the first-order terms, we have

$$\boldsymbol{\sigma} = -(p - \mu + \mu\varepsilon_b)\mathbf{I} + 2\mu\boldsymbol{\varepsilon} \quad (2.31)$$

Comparing Eq. 2.31Displacement, strain and stress fieldsequation.2.2.31 with the linear elasticity expression in Hall et al. [53], i.e.,

$$\boldsymbol{\sigma} = -\tilde{p}\mathbf{I} + 2\mu\boldsymbol{\varepsilon} \quad (2.32)$$

it can be seen that the p in Eq. 2.25Displacement, strain and stress fieldsequation.2.2.25 is not the same as the hydrostatic pressure $\tilde{p}$ in the linear stress-strain relation Eq. 2.32Displacement, strain and stress fieldsequation.2.2.32. The p and $\tilde{p}$ are related through

$$\tilde{p} = p - \mu + \mu\varepsilon_b. \quad (2.33)$$

With infinitesimal deformation, Eq. 2.28Displacement, strain and stress fieldsequation.2.2.28 reduces to

$$p(\mathbf{X}) - p(\mathbf{X}_0) \approx \mu \int_{\mathbf{X}_0}^{\mathbf{X}} (\nabla_X^2 \mathbf{u}) \cdot d\mathbf{s}. \tag{2.34}$$

Expressed in terms of $\tilde{p}$, Eq. 2.34Displacement, strain and stress fieldsequation.2.2.34 becomes

$$\tilde{p}(\mathbf{X}) - \tilde{p}(\mathbf{X}_0) \approx \mu \int_{\mathbf{X}_0}^{\mathbf{X}} (\nabla_X^2 \mathbf{u}) \cdot d\mathbf{s} + \mu[\varepsilon_b(\mathbf{X}) - \varepsilon_b(\mathbf{X}_0)] \tag{2.35}$$

which is exactly the same as Eq. 2.17Displacement, strain and stress fieldsequation.2.2.17 in Hall et al. [53].

2.3 Parameters

As described in Section 2.1Basic principlesection.2.1, there are four important parameters in the MLS method that can influence the interpolated displacement field. Here we briefly outline these parameters and their effects. Further discussions on these parameters will be made in Chapter 4Results for the indentation example and parametric studychapter.4.

The first parameter is the cut-off radius r_c. It defines the size of local domain Ω_b and therefore determines how many data points are used for interpolation. If the distance between a data point and the interpolation point (e.g. point A in Fig. 2.1Schematic diagram to demonstrate the weight of data points. In domain Ω (the purple square), A is a point whose displacement we are interested in. B_1, B_2 and B_3 are the data points near A. The yellow circle Ω_b centered at X differentiates the weight of data points. Only data points inside Ω_b contribute to the interpolation.figure.caption.9) is larger than r_c, this data point has zero weight in the interpolation. To minimize the numerical errors of interpolation, the cut-off radius r_c should not be too large or too small. An excessively large r_c may bring in data points that are far away from the interpolation point. A small r_c may lead to a Ω_b that is too small without enough data points in it to accurately determine

$a(\mathbf{X})$. In the extreme case where there are no data points inside Ω_b, all the elements of $\mathbf{A}(\mathbf{X})$ in Eq. 2.5Basic principleequation.2.1.5a are zero, so $\mathbf{A}^{-1}(\mathbf{X})$ becomes non-invertible and $\tilde{v}(\mathbf{X})$ can not be determined. Besides, it should be noted that the number of data points inside Ω_b should be larger than the length of the coefficients $a(\mathbf{X})$. Otherwise there will be multiple solutions for $a(\mathbf{X})$.

Secondly, the total number of data points n determines the density of data points inside Ω_b. If n is too small, the data points included in Ω_b may not be sufficient to yield accurate results for $a(\mathbf{X})$ and can also affect the smoothness of the interpolation fields. In Chapter 3Models and methodchapter.3, a quantity will be proposed to define the density of data points.

Thirdly, the weight function $f(\mathbf{X} - \mathbf{b}_I)$ determines how much every data point contributes to the weighted least-square error function L and influences the interpolation. Belytschko et al. [54] and Liu [63] provided various kinds of weight functions. Below are three frequently used weight functions,

Exponential:

$$f(\mathbf{X} - \mathbf{b}_I) = \begin{cases} \dfrac{exp(1 - d^2/r_c^2) - 1}{e - 1} & d \leq r_c \\ \\ 0 & d > r_c \end{cases} \tag{2.36a}$$

Conical:

$$f(\mathbf{X} - \mathbf{b}_I) = \begin{cases} 1 - (\dfrac{d}{r_c})^2 & d \leq r_c \\ \\ 0 & d > r_c \end{cases} \tag{2.36b}$$

Quartic spline:

$$f(\mathbf{X}-\mathbf{b}_I)=\begin{cases}1-6(\dfrac{d}{r_c})^2+8(\dfrac{d}{r_c})^3-3(\dfrac{d}{r_c})^4 & d\le r_c\\ \\ 0 & d>r_c\end{cases}\tag{2.36c}$$

where d equals $|\mathbf{X}-\mathbf{b}_I|$, the distance between a data point and the interpolation point, and r_c is cut-off radius. These weight functions share a common feature: they start at 1 and gradually decrease to 0 when d increases from 0 to r_c. For $d>r_c$, they are all zero. What will happen if a data point is located at the boundary of the yellow circle Ω_b in Fig. 2.1Schematic diagram to demonstrate the weight of data points. In domain Ω (the purple square), A is a point whose displacement we are interested in. B_1, B_2 and B_3 are the data points near A. The yellow circle Ω_b centered at X differentiates the weight of data points. Only data points inside Ω_b contribute to the interpolation.figure.caption.9, namely at $d=r_c$? First, since the data points are randomly distributed, it is a very rare event that a data point happens to be located at the boundary of the circular region Ω_b. It should be noted that the exponential and conical weight functions are not differentiable at $d=r_c$, since the derivatives using the branches on the left and right of $d=r_c$ are different. In our numerical program, we used the branch of the weight function at $d\le r_c$ to define the derivative of the weight function for data points located at $d=r_c$. In principle this may cause discontinuity in the spatial derivatives of the interpolation function as a certain data point enters or leaves the circular region Ω_b when Ω_b is relocated for different interpolation points. However, in practice, we did not observe any significant effects due to such discontinuity in our MLS results (e.g. see the indentation results in Chapter 4Results for the indentation example and parametric studychapter.4).

What's more, from Eq. 2.4Basic principleequation.2.1.4 and Eq. 2.5Basic principleequation.2.1.5, one can see that the solution of coefficients $a(\mathbf{X})$ is not affected by the absolute value of the weight function, but rather by its relative distribution. These three weight functions are plotted in Fig. 2.2Plots of conical, exponential and quartic spline weight functions. Horizontal axis represents d/r_c and the vertical axis is the value of weight function. The solid line is the conical function. The dashed one is the exponential function and the dotted line is the quartic spline function. figure.caption.10. It is seen that conical weight function shows the slowest decay among these three functions. If the density of the available data points is relatively low, the exponential and quartic spline weight functions may lead to a scenario where only a few data points close to the interpolation point contribute to the weighted least-square error function L. In this case, the conical function may yield better results by effectively taking more data points into account for L. On the contrary, if the density of data points is high, the conical function may not perform as well as the other two. In practice, lower data points density can lead to simpler experimental procedures and reduce computational cost. Due to these advantages, we will focus on the conical weight function. Besides, we also compare the effect of conical weight function with exponential weight function. The quartic spline weight function, although not implemented in this study, has been shown to yield accurate results for crack growth problems when used in the mesh free method [64]. We expect that this is also a promising weight function for our application and the testing of its performance is a subject of future study.

Finally, we are going to discuss the interpolation basis $\mathbf{P}^T(\mathbf{X})$. Here we consider three typical types of polynomial basis functions shown below:

$$\begin{aligned}
\text{linear:}\quad & \mathbf{P}^T(\mathbf{X}) = [1, X_1, X_2, X_3] \\
\text{quadratic:}\quad & \mathbf{P}^T(\mathbf{X}) = [1, X_1, X_2, X_3, X_1X_2, X_2X_3, X_1X_3, X_1^2, X_2^2, X_3^2] \\
\text{cubic:}\quad & \mathbf{P}^T(\mathbf{X}) = [1, X_1, X_2, X_3, X_1X_2, X_2X_3, X_1X_3, X_1^2, X_2^2, X_3^2, \\
& \qquad X_1X_2X_3, X_1^2X_2, X_1^2X_3, X_2^2X_1, X_2^2X_3, X_3^2X_1, X_3^2X_2, \\
& \qquad X_1^3, X_2^3, X_3^3]
\end{aligned}$$

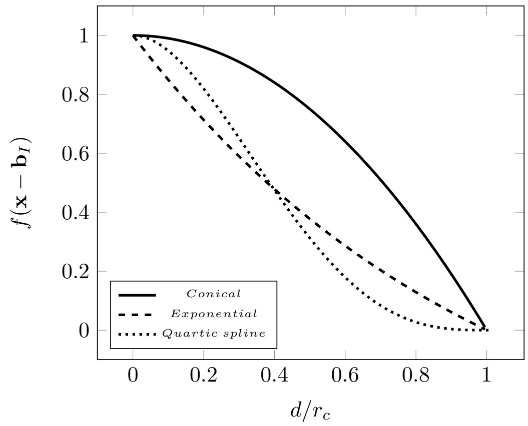

Fig. 2.2. Plots of conical, exponential and quartic spline weight functions. Horizontal axis represents d/r_c and the vertical axis is the value of weight function. The solid line is the conical function. The dashed one is the exponential function and the dotted line is the quartic spline function.

According to Eq. 2.6Basic principleequation.2.1.6, if interpolation basis $\mathbf{P}^T(\mathbf{X})$ is a $1 \times m$ vector, it requires the coefficient $a(\mathbf{X})$ to be a $m \times 1$ vector. This means that if the cubic basis is used, the computational cost is higher and more data points are needed in the local influential zone Ω_b as compared to the other two basis functions. However, it is also expected that cubic basis can result in a more accurate and smooth field $\tilde{v}(\mathbf{X})$ after interpolation.

Chapter 3

Models and method

3.1 Models

To investigate the accuracy of MLS in constructing continuous fields and the effects of the four parameters, three examples are introduced, including an indentation model with a rigid spherical indenter on a soft elastic layer, a plane stress plate with a circular hole under uni-axial tension, and a plane stress crack under symmetric (Mode I) loading.

Fig. 3.1afigure.caption.11 shows the cross-section of the indentation model: a rigid spherical indenter with radius R on a soft gel layer. Axisymmetry of indentation model allows us to consider a cross-section of the gel layer which is shown as a $h \times w$ rectangle, where h is the thickness and w is the width. The indenter-gel interface is assumed to be frictionless. A vertical downward displacement of δ (indentation depth) is applied to the indenter, causing the gel to deform. The width w of the gel is assumed to be much larger than its height h and the indenter radius R so that the gel can be regarded as infinitely wide, i.e., deformation of the gel is not affected by the lateral boundary. The dashed lines illustrates the deformed configuration of gel upon indentation. The small rectangle filled by red lines (it is in the undeformed configuration) is where the displacement, strain and stress fields are computed, namely Ω in Fig. 2.1Schematic diagram to demonstrate the weight

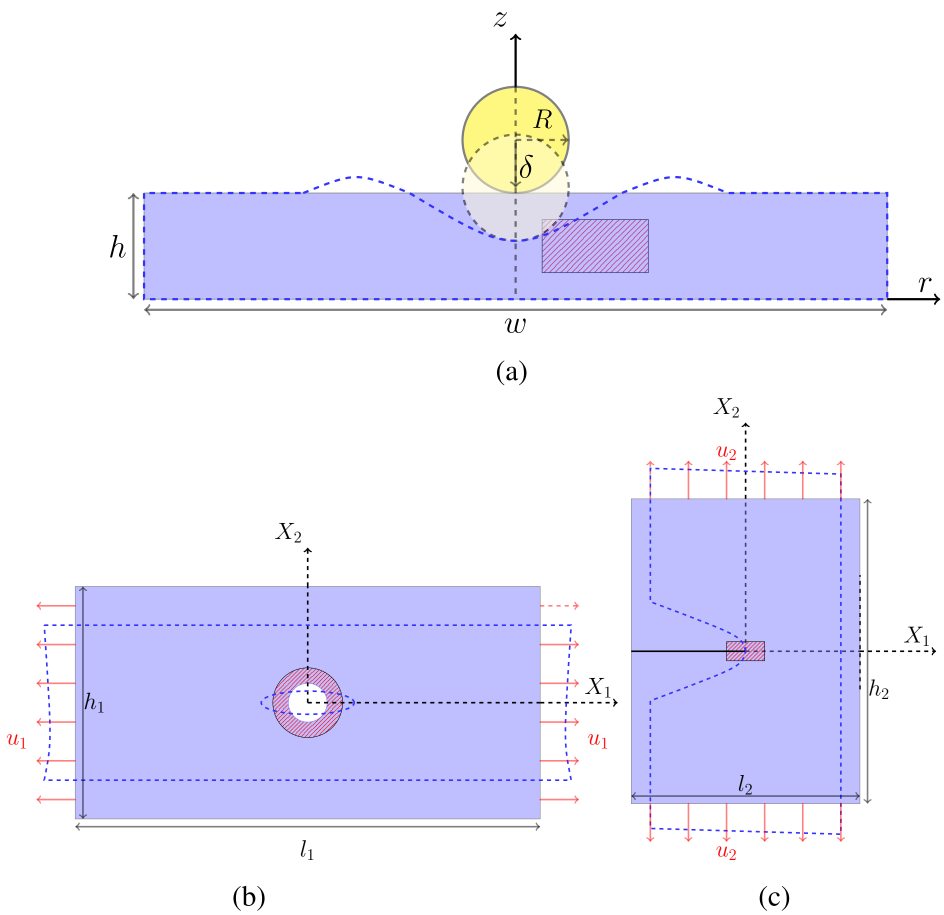

Fig. 3.1. Schematics of models studied in this work. (a) cross-section of a rigid sphere indenting a layer of gel. Shape after deformation is approximated by the dashed lines. (b) a plate with a hole is stretched in the horizontal direction by the applied displacement u_1. (c) an edge crack opened in the vertical direction by the constant displacement u_2. The red shaded regions in all subfigures are the areas of interest, i.e., Ω in Fig. 2.1Schematic diagram to demonstrate the weight of data points. In domain Ω (the purple square), A is a point whose displacement we are interested in. B_1, B_2 and B_3 are the data points near A. The yellow circle Ω_b centered at X differentiates the weight of data points. Only data points inside Ω_b contribute to the interpolation.figure.caption.9.

of data points. In domain Ω (the purple square), A is a point whose displacement we are interested in. B_1, B_2 and B_3 are the data points near A. The yellow circle Ω_b centered at X differentiates the weight of data points. Only data points inside Ω_b contribute to the interpolation.figure.caption.9.

The indentation model is the benchmark problem to assess the accuracy of MLS and the effects of the four parameters. This is because that the indentation example has been experimentally implemented in Hall et al. [53] to demonstrate the particle-tracking based method (with MLS interpolation) for full-field mapping of the displacement, strain and stress. Using this model as the benchmark has two advantages here:1) the axis-symmetric geometry is suitable for testing the 3D capability of MLS method instead of using a 3D FEA model which is computationally expensive; 2) the non-uniform deformation due to indentation can help test if MLS method yields smooth strain and stress fields.

After the optimized set of parameters is obtained from the indentation model, we can apply it into two additional examples with severe stress concentration. The purpose is to evaluate the possibility of using particle tracking based method (with MLS interpolation) to experimentally measure the deformation and stress fields in cases with defects such as cavity and crack.

Fig. 3.1bfigure.caption.11 and Fig. 3.1cfigure.caption.11 show the two models with defects. A circular hole with radius r_1 is located at the center of a thin plate (see Fig. 3.1bfigure.caption.11). The dimensions of the plate is $l_1 \times h_1$, where l_1 is the length and h_1 is the height. A horizontal displacement u_1 is applied at the left and right edges of the plate, so that the plate is under uni-axial stretch. The dashed lines illustrate the deformed configuration of the plate. Our zone of interest is the red annular region where the stress concentration is located. In Fig. 3.1cfigure.caption.11, an edge crack of length $q/2$ is located in the middle of a $l_2 \times h_2$ plate (l_2 is the length and h_2 is the height). A vertical displacement u_2 is applied on both the top and bottom boundaries of the plate to open the crack. The red rectangle surrounding the crack tip will experience extremely large local stress, which is our zone of interest.

3.2 Simulation details

3.2.1 Dimensions and boundary conditions

The deformation of three models were simulated using a commercial finite element software ABAQUS (version 6.13, Dassault Systemes Simulia Corp., Providence, RI). Table. 3.1Finite element simulation details.table.caption.12 summarizes details regarding dimensions of the finite element models, boundary conditions and applied loadings.

For the indentation model shown in Fig. 3.1afigure.caption.11, the gel layer is modelled as a deformable body and meshed by axisymmetry elements CAX4RH. The height of the gel is h and the length of it is $40h$. Because of the axisymmetry, boundary O_1C_1 (see Table. 3.1Finite element simulation details.table.caption.12) is fixed in r direction. The bottom O_1A_1 is fixed in all directions. The indenter is modelled as a rigid object. An indentation depth $\delta = 0.2532h$ is assigned on the indenter, forcing the gel to deform. The value of $0.2532h$ is consistent with the work of Hall et al. [53]. To study the effects of large deformation on the indentation model, we run two simulation jobs in ABAQUS by applying a test loading $\delta = 0.5h$. The difference of the two jobs lies in the switch of Nlgeom accounting for the geometrical nonlinearity. The details of why we did three loadings will be further illustrated in the next section.

For the second case shown in Fig. 3.1bfigure.caption.11, a quarter of the plate is modelled and meshed by CPS4 elements. The length of the plate is 80 and the height is 40. The radius of the hole is 2. Finer mesh is used around the hole where the zone of interest is located. Because of symmetry, the left boundary O_2D_2 can-

TABLE 3.1

FINITE ELEMENT SIMULATION DETAILS.

<table>
<tr><td>
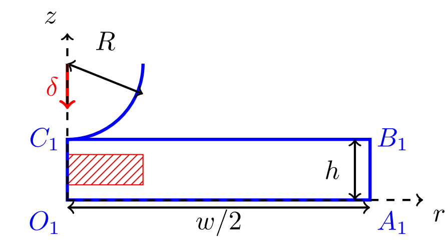

</td><td>$h = 1$ $R = 4.366h$ $w/2 = 20h$
CAX4RH elements
test loading 1:
$\delta = 0.5h$ (Nlgeom: off)
test loading 2:
$\delta = 0.5h$ (Nlgeom: on)
loading 3:
$\delta = 0.2532h$ (Nlgeom: on)
Axisymmetric problem</td></tr>
<tr><td>
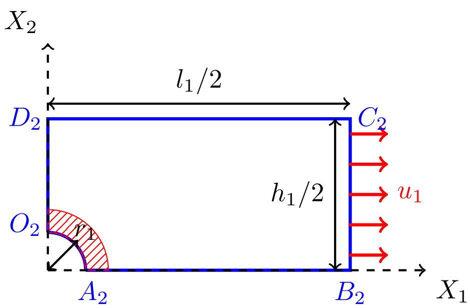

</td><td>$l_1/2 = 40$ $h_1/2 = 20$ $r_1 = 2$
CPS4 elements
loading 1:
u_1= 20 (Nlgeom: on)
loading 2:
u_1= 40 (Nlgeom: on)
Plane stress problem</td></tr>
<tr><td>
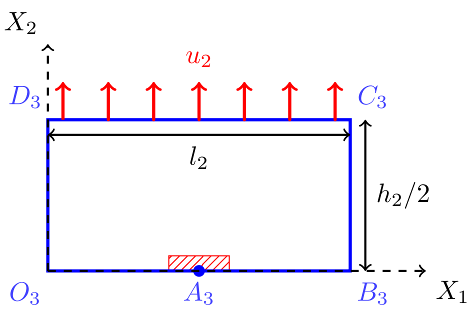

</td><td>$l_2 = 20$ $h_2/2 = 10$ $q = 0.02$
CPS4 elements
loading 1:
u_2= 5 (Nlgeom: on)
loading 2:
u_2= 10 (Nlgeom: on)
Plane stress problem</td></tr>
</table>

not move in X_1 direction and the bottom boundary A_2B_2 is fixed in X_2 direction. Constant displacement u_1 is added to the right side B_2C_2. There are two options about u_1: $u_1 = 20$ and $u_1 = 40$.

For the last model shown in Fig. 3.1cfigure.caption.11, we took advantage of symmetry and modelled the top half of the plate in ABAQUS. The length of the plate is 20 and the height is 20. The mesh element type is CPS4. The boundary O_3A_3 is traction free and the boundary A_3B_3 is fixed in X_2 direction (see Table. 3.1Finite element simulation details.table.caption.12). A displacement u_2 is applied on the top D_3C_3, forcing the crack to open. The mesh size decreases as the crack tip A_3 is approached to resolve the highly concentrated deformation and stress. The largest elements size away from the crack tip is 0.5 and the smallest one close to the crack tip is 0.0006.

3.2.2 Material properties

We adopted the incompressible neo-Hookean material model, one of the simplest hyper-elastic material models, for the three cases described in Section 3.2Simulation detailssection.3.2.1. This is because the loadings we applied can cause very large deformation. For example, in the plane stress crack problem (see the third row of Table. 3.1Finite element simulation details.table.caption.12), the total applied displacement $2u_2$ (on both top and bottom edges) is as large as 100% of the height q. Similar range of large loadings are also used in the circular hole problem (see the second row of Table. 3.1Finite element simulation details.table.caption.12). In addition, the geometrical nonlinearity is accommodated by turning the switch of "Nlgeom" in ABAQUS.

We normalize the shear modulus μ by the Young's modulus E:

$$\mu^* = \frac{\mu}{E} = \frac{1}{2(1+\upsilon)} \tag{3.1}$$

where μ is shear modulus, E is Young's modulus and υ is the Poisson's ratio. For incompressible material, υ is equal to 0.5. Therefore,

$$\mu^* = \frac{1}{3} \tag{3.2a}$$

$$C_1^* = \frac{\mu^*}{2} = \frac{1}{6} \tag{3.2b}$$

where C_1^* is the normalized form of material constant $C_1 = \frac{\mu}{2}$.

For the indentation model, we used an indentation depth of $\delta = 0.2532h$. This is the same as the indentation depth used by Hall et. al [53] in their experiments

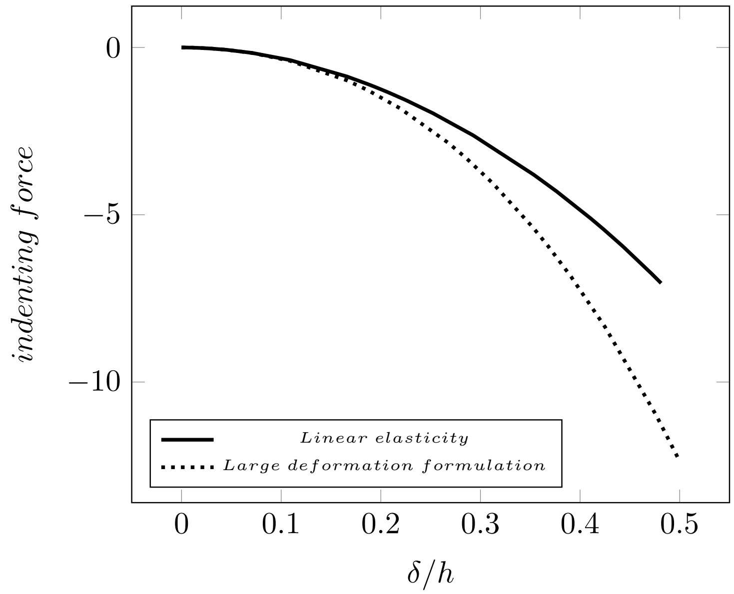

Fig. 3.2. The indenting force versus indentation depth. The solid line is plotted when Nlgoem switch is turned off. The dotted line is plotted when Nlgoem switch is turned on.

to demonstrate the particle-tracking based full-field mapping of deformation and stress. Note that Hall et al.[53] adopted linear elastic theory to calculate strain and stress fields due to indentation. However, given $\delta = 0.2532h$ is about 25% of the gel thickness h, it is not immediately clear how strong the large deformation effects are. Therefore, we conducted two different FEA simulations to explore the effects of large deformation in our indentation model. In one simulation, we use a linear elastic material model with the Young's modulus E and the Poisson's ratio $\upsilon = 0.5$ (incompressible) and turned the geometrical nonlinearity switch "Nlgeom" off, while in the other simulation, we use an incompressible neo-Hookean model with the same Young's modulus and turned "Nlgeom" switch on. In both simulations, we gradually increase the indentation depth δ from 0 to $0.5h$, and extract the indenting force as a function of the indentation depth δ. By comparing the force-indentation depth curves from these two simulations, we are able to see at which point the large deformation effects become clear. Fig. 3.2The indenting force versus indentation depth. The solid line is plotted when Nlgoem switch is turned off. The dotted line is plotted when Nlgoem switch is turned on.figure.caption.13 plots the force-indentation depth results from the two simulations. The horizontal axis is the normalized indentation depth δ/h, and the vertical axis is indenting force. The force is negative because it is compressive. It is seen that the solid line (linear elasticity) and the dotted line (large deformation formulation) begin to deviate from each other when indentation depth δ reaches approximately $0.18h$. When indentation depth $\delta = 0.2532h$, the large deformation formulation results in an indenting force almost 25% larger than the linear elasticity result. From this comparison, we conclude that at $\delta = 0.2532h$, the large deformation effect is not negligible, and neo-Hookean material together with geometrical nonlinearity should be used.

After the jobs in ABAQUS are completed, the nodal displacements in the zone of interest will be extracted as the input for the MLS interpolation to get displacement and strain fields. For the calculation of stress fields, the same neo-Hookean material model will be used to be consistent with the FEA model. Then all the displacement, strain and stress fields given be MLS will be compared with those from FEA to assess the accuracy of MLS.

It needs to be pointed out that there are many other hyper-elastic material models (e.g. Arruda Boyce model, Gent model and Ogden model [65]) available. To determine which model to be used in experiments, one needs to conduct additional mechanical testings (e.g. uni-axial tension or compression and bi-axial tension tests). Here since our focus is to study the accuracy of MLS interpolation method, we have chosen a simplest material model (neo-Hookean) but the formulation can be easily extended to other more sophisticated hyper-elastic models.

3.3 Expressions of strain and stress components

In Section 2.2Displacement, strain and stress fieldssection.2.2, we present the general equations of true strain and Cauchy stress in Cartesian coordinates. In this section, we will list the specific calculations of the strain and stress using the displacement interpolated from MLS.

The indentation model shown in Fig. 3.1afigure.caption.11 is axisymmetric. The displacement extracted from the FEA results is in terms of cylindrical coordinates r, θ and z (see Fig. 3.3Cylinderical coordinates and Cartesian coordinates.figure.caption.14). Here we show how to adapt the three-dimensional formulation presented in Section 2.2Displacement, strain and stress fieldssection.2.2, which is in Cartesian coordinates, to cylindrical coordinates. The displacement vector in cylindrical coordinates

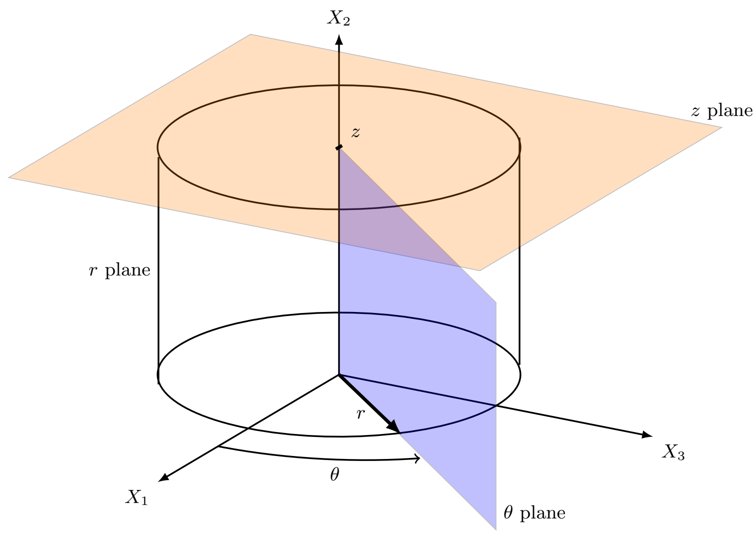

Fig. 3.3. Cylinderical coordinates and Cartesian coordinates.

is:

$$\mathbf{u}^T = [u_r, u_\theta, u_z] \tag{3.3}$$

where u_r, u_θ and u_z are the displacements in r, θ and z directions. Due to axisymmetry, u_θ is zero everywhere and u_r, u_z are independent of coordinate θ. The components of deformation gradient $\mathbf{F}$ in cylindrical coordinates can be expressed as [66]:

$$\mathbf{F} = \begin{bmatrix} F_{rr} & F_{r\theta} & F_{rz} \\ F_{\theta r} & F_{\theta\theta} & F_{\theta z} \\ F_{zr} & F_{z\theta} & F_{zz} \end{bmatrix} = \begin{bmatrix} 1 + \dfrac{\partial u_r}{\partial r} & \dfrac{1}{r}\dfrac{\partial u_r}{\partial \theta} - \dfrac{u_\theta}{r} & \dfrac{\partial u_r}{\partial z} \\ \dfrac{\partial u_\theta}{\partial r} & 1 + \dfrac{1}{r}\dfrac{\partial u_\theta}{\partial \theta} + \dfrac{u_r}{r} & \dfrac{\partial u_\theta}{\partial z} \\ \dfrac{\partial u_z}{\partial r} & \dfrac{1}{r}\dfrac{\partial u_z}{\partial \theta} & \dfrac{\partial u_z}{\partial z} \end{bmatrix} = \begin{bmatrix} 1 + \dfrac{\partial u_r}{\partial r} & 0 & \dfrac{\partial u_r}{\partial z} \\ 0 & 1 + \dfrac{u_r}{r} & 0 \\ \dfrac{\partial u_z}{\partial r} & 0 & 1 + \dfrac{\partial u_z}{\partial z} \end{bmatrix} \tag{3.4}$$

The axisymmetry also allows us to just consider any cross-section of the gel spanned by the r and z axes instead of a full 3D domain. This is also how the FEA results are presented. For convenience, we consider a cross-section and treat the r and z axes, which are orthogonal, as two in-plane Cartesian axes. In other words, we name the r coordinate as X_1, the z axe as X_2 and the θ direction as the X_3 direction (see Fig. 3.3Cylinderical coordinates and Cartesian coordinates.figure.caption.14). In this way, components of the deformation gradient can be rearranged into the following form:

$$\mathbf{F} = \begin{bmatrix} F_{11} & F_{12} & 0 \\ F_{21} & F_{22} & 0 \\ 0 & 0 & F_{33} \end{bmatrix} = \begin{bmatrix} 1 + \dfrac{\partial u_r}{\partial r} & \dfrac{\partial u_r}{\partial z} & 0 \\ \dfrac{\partial u_z}{\partial r} & 1 + \dfrac{\partial u_z}{\partial z} & 0 \\ 0 & 0 & 1 + \dfrac{u_r}{r} \end{bmatrix}$$
$$= \begin{bmatrix} 1 + \dfrac{\partial u_1}{\partial X_1} & \dfrac{\partial u_1}{\partial X_2} & 0 \\ \dfrac{\partial u_2}{\partial X_1} & 1 + \dfrac{\partial u_2}{\partial X_2} & 0 \\ 0 & 0 & 1 + \dfrac{u_1}{X_1} \end{bmatrix} \tag{3.5}$$

It is noteworthy that the in-plane components of deformation gradient **F** have no difference from those of a plane-stress or plane-strain problem. However, the out-of-plane component F_{33} is not zero even though the displacement component $u_3 = 0$ (u_θ in cylindrical coordinates). This is because of the axisymmetric geometry. Given the transformation of **F** from cylindrical coordinates to Cartesian coordinates, one can easily compute the strain from Eq. 2.18Displacement, strain and stress fieldsequation.2.2.18 and Eq. 2.19Displacement, strain and stress fieldsequation.2.2.19.

As to the expressions for stress, according to Eq. 2.25Displacement, strain and stress fieldsequation.2.2.25, it can be shown as

$$\sigma_{11} = -p + \frac{\mu}{J} B_{11} \tag{3.6a}$$
$$\sigma_{12} = \frac{\mu}{J} B_{12} \tag{3.6b}$$
$$\sigma_{22} = -p + \frac{\mu}{J} B_{22} \tag{3.6c}$$

While the components of left Cauchy Green deformation tensor **B** can be computed from Eq. 2.20cDisplacement, strain and stress fieldsequation.2.2.3, the key to calculate stress is to determine the hydrostatic pressure p in Eq. 3.6Expressions of strain and stress componentsequation.3.3.6a and Eq.3.6Expressions of strain and stress componentsequation.3.3.6c. Refer Eq. 2.28Displacement, strain and stress fieldsequation.2.2.28, the hydrostatic pressure of an interpolation point is related to the integration of $\frac{1}{J}(\nabla_X^2\mathbf{u})\cdot(\mathbf{F}d\mathbf{s})$. For the axisymmetric indentation model, we have

$$\nabla_X^2\mathbf{u}=\left(\frac{\partial^2 u_r}{\partial r^2}+\frac{1}{r}\frac{\partial u_r}{\partial r}+\frac{\partial^2 u_r}{\partial z^2}-\frac{u_r}{r^2}\right)\mathbf{e}_r+\left(\frac{\partial^2 u_z}{\partial r^2}+\frac{1}{r}\frac{\partial u_z}{\partial r}+\frac{\partial^2 u_z}{\partial z^2}\right)\mathbf{e}_z \quad (3.7)$$

where $\mathbf{e}_r$ and $\mathbf{e}_z$ are basis vectors for the cylindrical coordinates. Based on the axisymmetry, the integral in Eq. 2.28Displacement, strain and stress fieldsequation.2.2.28 is done in the $r-z$ plane, namely

$$d\mathbf{s}=(ds)_r\mathbf{e}_r+(ds)_z\mathbf{e}_z \quad (3.8)$$

Therefore,

$$\mathbf{F}d\mathbf{s}=(F_{rr}(ds)_r+F_{rz}(ds)_z)\mathbf{e}_r+(F_{zr}(ds)_r+F_{zz}(ds)_z)\mathbf{e}_z \quad (3.9)$$

As a result, the integral term becomes

$$\begin{aligned}\frac{1}{J}(\nabla^2\mathbf{u})\cdot(\mathbf{F}d\mathbf{s})=&\frac{1}{J}[F_{rr}(\frac{\partial^2 u_r}{\partial r^2}+\frac{1}{r}\frac{\partial u_r}{\partial r}+\frac{\partial^2 u_r}{\partial z^2}-\frac{u_r}{r^2})(ds)_r\\&+F_{zr}(\frac{\partial^2 u_z}{\partial r^2}+\frac{1}{r}\frac{\partial u_z}{\partial r}+\frac{\partial^2 u_z}{\partial z^2})(ds)_r\\&+F_{rz}(\frac{\partial^2 u_r}{\partial r^2}+\frac{1}{r}\frac{\partial u_r}{\partial r}+\frac{\partial^2 u_r}{\partial z^2}-\frac{u_r}{r^2})(ds)_z\\&+F_{zz}(\frac{\partial^2 u_z}{\partial r^2}+\frac{1}{r}\frac{\partial u_z}{\partial r}+\frac{\partial^2 u_z}{\partial z^2})(ds)_z]\end{aligned} \quad (3.10)$$

The rest is to change $r\rightarrow 1$, $\theta\rightarrow 3$ and $z\rightarrow 2$. Then we have the equation of calculating Cauchy stress from cylindrical coordinates to Cartesian coordinates.

For the other two models, i.e., thin plate with a hole and Mode-I crack, plane stress condition is assumed. Let X_3 be the out of the plane axis. The plane stress condition means that the stress components σ_{13}, σ_{23} and σ_{33} all banish. The in-plane components of strain and stress can be calculated following Section 2.2Displacement, strain and stress fieldssection.2.2 since the two models are in Cartesian coordinates.

3.4 Evaluation of the accuracy of MLS interpolation

Given the displacement, strain and stress fields from MLS and FEA, the next is to assess the accuracy of MLS. Therefore, in this section, we are going to define quantitative measurements of the accuracy of MLS.

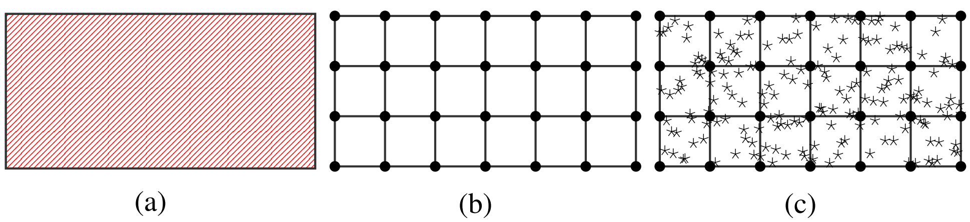

Fig. 3.4. Schematics of zone of interest in different forms. (a) Zone of interest itself shaded by red lines. (b) Zone of interest divided into grids. The black circles are gird points. (c) Zone of interest containing grid points and data points inside. Data points are marked by stars.

As shown in Table. 3.1Finite element simulation details.table.caption.12, a zone of interest is selected for each model. Take the zone of interest of indentation model as an example. Its schematic is shaded in red in Fig. 3.4afigure.caption.15. We divided the zone of interest into grids (see Fig. 3.4bfigure.caption.15) and named the intersections as grid points. It should be pointed out that the zone of interest is presented in the undeformed configuration. This is because when the material undergoes large deformation, the deformed shape of the zone of interest may become highly distorted, especially for the plane stress crack example (see Chapter 5Application cases with stress concentrationchapter.5). If the zone of interest is presented in the deformed configuration, it may be difficult to visualize the stress field in the deformed zone of interest.

As described earlier, we extract displacements at a set of data points from the FEA results and use these data points as the input for the MLS interpolation to compute the displacement, strain and stress at each of the grid point. A schematic of the grid point (black dots) and the data points (stars) is shown in Fig. 3.4cfigure.caption.15. The results from MLS interpolation are then compared with those from the FEA model so that the accuracy of MLS can be evaluated. We emphasize that in experiments (e.g. see Hall et al. [53]), the displacements of data points were obtained by tracking fluorescent beads embedded in the material. Here our focus is to evaluate the accuracy of MLS interpolation, and thus we pick the data points directly from the FEA model. To simulate the random distribution of the data points in experiments, we use a random number generator in MATLAB program (MATLAB, The MathWorks, Natick, MA) to generate a list of nodes inside the zone of interest and use these as our data points.

The next question is how to quantitatively evaluate the overall accuracy of the MLS method. We compare the MLS and FEA results at each of the grid point, and the overall accuracy of the MLS method is reflected as some collective measure of the relative errors at each grid point. One natural choice is the average of the relative errors at all the grid points. Take the displacement field as an example, the average relative error is defined as:

$$\eta_{ave} = \frac{\sum_{i=1}^{N} \eta_i}{N} \tag{3.11}$$

where

$$\eta_i = |\frac{u_i - u_{mls,i}}{u_i}| \times 100\%, \tag{3.12}$$

N represents the total number of grid points in zone of interest, u_i means the exact displacement (from FEA) of the i^{th} grid point, $u_{mls,i}$ is the interpolated displacement (from MLS) of the i^{th} grid point and η_i refers to the relative error between them. Similar η_i can be defined for calculating the relative error of strain and stress components. However, the average relative error may not faithfully reflect the overall accuracy of MLS since it can be easily distorted by a few grid points with extremely large relative errors η_i, such as when u_i is close to zero. Therefore we use an alternative measure, i.e., the median of the relative errors at all the grid points:

$$\tilde{\eta} = \text{Median of } \{\eta_1, \eta_2, ..., \eta_N\} \tag{3.13}$$

where $\eta_i(i = 1, 2, ..., N)$ is defined in Eq. 3.12Evaluation of the accuracy of MLS interpolationequation.3.4.12 and median is the number separating the higher half of $\eta_i(i = 1, 2, ..., N)$.

TABLE 3.2
PARAMETERS USED IN MLS INTERPOLATION AND ZONE OF INTEREST FOR EACH MODEL.

models	number of data points	interpolation basis	cut-off radius	weight function	zone of interest
indentation	180 300 500 600 800 1000 2000	linear quadratic cubic	0.2 0.3 0.4 0.5 0.6 0.7	conical exponential for several groups	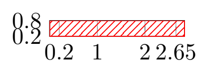
tension	200 800	cubic	0.7	conical	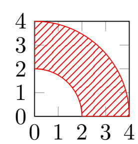
crack	200 800	cubic	0.005	conical	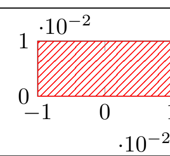

To explore how the four parameters listed in Section 2.3Parameterssection.2.3 affect the accuracy of the MLS interpolation results, we conducted a parametric study by varying these parameters and comparing the resulting median relative error $\tilde{\eta}$. Table. 3.2Parameters used in MLS interpolation and zone of interest for each model.table.caption.16 list the specific parameters used in MLS interpolation for three models. In the second row of Table. 3.2Parameters used in MLS interpolation and zone of interest for each model.table.caption.16, it is indicated that for the indentation model, we considered seven values for total number of data points, three kinds of interpolation bases and six types of cut-off radius. Therefore, we have $7 \times 3 \times 6 = 126$ different combinations of MLS parameters when the choice of conical weight function is fixed (in section. 2.3Parameterssection.2.3 it is mentioned that conical weight function is the main weight function used). Through computing the median $\tilde{\eta}$ in Eq. 3.13Evaluation of the accuracy of MLS interpolationequation.3.4.13 of each combination of parameters, we were able to see how $\tilde{\eta}$ can be influenced by each parameter (total number of data points, interpolation basis and cut-off radius). Besides that, we selected the combination of 1200 data points, cubic basis and cut-off radius $r_c = 0.4$ with exponential weight function to see the effect of weight function. It should be noted that the cut-off radius r_c are of different magnitude among the three models (see the forth column of Table .3.2Parameters used in MLS interpolation and zone of interest for each model.table.caption.16). This is because the size of zone of interest are quite different (see the sixth column of Table .3.2Parameters used in MLS interpolation and zone of interest for each model.table.caption.16).

Finally, we propose a normalized nearest neighbour distance as an alternative measure of the number of data points as follows:

$$\begin{aligned} \gamma &= \frac{d_{ave}}{\sqrt{S}} \\ &= \frac{\sum\limits_{i=1}^{n} \min\left\{\left|\mathbf{b}_i - \mathbf{b}_{j(j=1,2,3\ldots n; j\neq i)}\right|\right\}}{n\sqrt{S}} \end{aligned} \tag{3.14}$$

where n is the total number of data points, $\mathbf{b}_i$ and $\mathbf{b}_j$ represent the position vectors of the i^{th} and j^{th} data point, $|\mathbf{b}_i - \mathbf{b}_j|$ is the distance between them and S is the area of zone of interest. For a certain grid point at $\mathbf{b}_i$, min $\left\{\left|\mathbf{b}_i - \mathbf{b}_{j(j=1,2,3\ldots n; j\neq i)}\right|\right\}$ is the minimum distance between this data point and other data points located in the zone of interest. A set owning n elements can be formed by documenting min $\{|\mathbf{b}_i - \mathbf{b}_j|\}$. γ is obtained by taking the average of the set and then divided by $\sqrt{S}$. Then γ becomes a dimensionless parameter which is not supported by using the total number of data points. Another advantage of γ to the number of data points is that γ can easily be extended to 3D domain, but the number of data points for 2D or 3D domains cannot be directly compared (a sphere usually include more data points than a circle with the same radius). Table. 3.3Normalized nearest neighbour distance γ corresponding to the total number of data points.table.caption.17 lists the normalized nearest neighbour distance corresponding to the total number of data points for the indentation model.

TABLE 3.3
NORMALIZED NEAREST NEIGHBOUR DISTANCE γ CORRESPONDING TO THE TOTAL NUMBER OF DATA POINTS.

n	180	300	500	600	800	1000	1200	2000
d_{ave}	0.0479	0.038	0.0292	0.0272	0.024	0.0216	0.0199	0.0165
γ	0.0395	0.0313	0.0241	0.0224	0.0198	0.0178	0.0164	0.0136

For the two plane stress examples shown in Fig. 3.1bfigure.caption.11 and 3.1cfigure.caption.11, we did not perform an extensive parametric study as that for the indentation example. Instead, the parameters for MLS interpolation were selected based on the understandings learned from the indentation example. These parameters are shown in Table 3.2Parameters used in MLS interpolation and zone of interest for each model.table.caption.16. Our goal for these two examples is to see if the MLS method can accurately recover the strain and stress fields when there is severe stress concentration.

Chapter 4

Results for the indentation example and parametric study

The results of the indentation model and parametric study are included in this chapter. Specifically, in Section 4.1Displacement fieldsection.4.1, 4.2Strain fieldsection.4.2 and 4.3Stress fieldsection.4.3 we are going to present the displacement, strain and stress fields from MLS and discuss the effects of the normalized nearest neighbour distance, interpolation basis and cut-off radius. The effect of weight functions is illustrated in Section 4.4Effect of weight functionsection.4.4. Section 4.5Conclusionssection.4.5 summarizes the qualitative guideline regarding the selection of parameters for the MLS method.

4.1 Displacement field

Examples of the displacement fields u_1 and u_2 calculated from the MLS interpolation are shown in Fig. 4.1Displacement fields for the zone of interest from FEA and MLS. (a) and (b): contour plots of the continuous displacement field u_1. (c) and (d): contour plots of the continuous displacement field u_2. $\tilde{\eta}$ is the median of relative errors defined in Eq. 3.13Evaluation of the accuracy of MLS interpolationequation.3.4.13. Horizontal and vertical axes are $X_!$ and X_2 coordi-

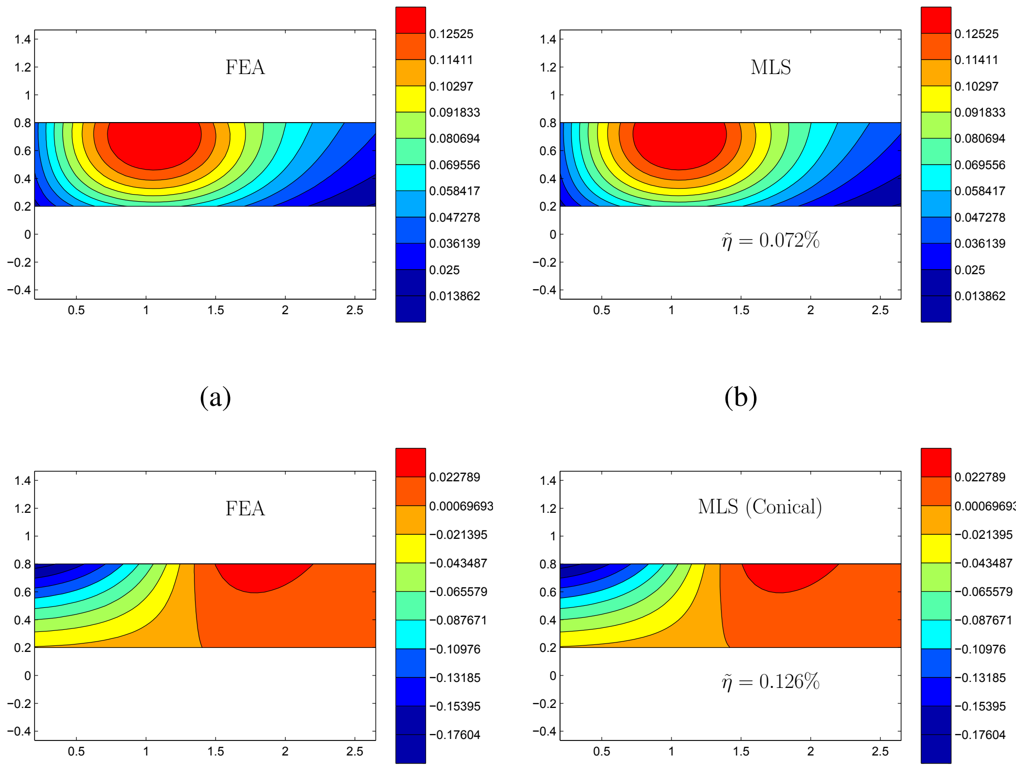

(a) (b)

(c) (d)

Fig. 4.1. Displacement fields for the zone of interest from FEA and MLS. (a) and (b): contour plots of the continuous displacement field u_1. (c) and (d): contour plots of the continuous displacement field u_2. $\tilde{\eta}$ is the median of relative errors defined in Eq. 3.13Evaluation of the accuracy of MLS interpolationequation.3.4.13. Horizontal and vertical axes are $X_!$ and X_2 coordinates, which indicate the position of zone of interest.

nates, which indicate the position of zone of interest.figure.caption.18b and 4.1Displacement fields for the zone of interest from FEA and MLS. (a) and (b): contour plots of the continuous displacement field u_1. (c) and (d): contour plots of the continuous displacement field u_2. $\tilde{\eta}$ is the median of relative errors defined in Eq. 3.13Evaluation of the accuracy of MLS interpolationequation.3.4.13. Horizontal and vertical axes are $X_!$ and X_2 coordinates, which indicate the position of zone of interest.figure.caption.18d, respectively. The parameters used are 800 data points ($\gamma = 0.0198$), cubic interpolation basis, cut-off radius $r_c = 0.4$ and conical weight function. Fig. 4.1afigure.caption.18 and Fig. 4.1cfigure.caption.18 plots the corresponding displacement fields from FEA results. As previously discussed, we use the FEA displacement fields as the reference to calculate numerical errors of the MLS method. For representative results in Fig. 4.1Displacement fields for the zone of interest from FEA and MLS. (a) and (b): contour plots of the continuous displacement field u_1. (c) and (d): contour plots of the continuous displacement field u_2. $\tilde{\eta}$ is the median of relative errors defined in Eq. 3.13Evaluation of the accuracy of MLS interpolationequation.3.4.13. Horizontal and vertical axes are $X_!$ and X_2 coordinates, which indicate the position of zone of interest.figure.caption.18, the median relative error $\tilde{\eta}$ are found to be $0.072\%$and 0.126% for u_1 and u_2, respectively, which demonstrates that the MLS method is capable of very accurately reproducing a continuous displacement field from the given data points.

To explore how the MLS interpolation results are affected by the parameters discussed in Section 2.3Parameterssection.2.3, we calculated the median relative error $\tilde{\eta}$ for every combinations of the parameters listed in Table. 3.2Parameters used in MLS interpolation and zone of interest for each model.table.caption.16 except the weight function. We have used the conical weight function for all the results presented here. The effect of using different weight functions is briefly discussed in Section 4.4Effect of weight functionsection.4.4. Fig. 4.2Evaluation of MLS approximating u_2 (displacement in X_2 direction). (a), (b) and (c) are the plots of $\tilde{\eta}$ versus γ using different interpolation basis. (a): Linear basis. (b): Quadratic basis. (c): Cubic basis. (a), (b) and (c) have the same legend meaning the employed cut-off radius for each MLS interpolation.figure.caption.19 plots the median relative errors $\tilde{\eta}$ for the displacement component u_2 with different MLS parameters. We choose u_2 because it was found to exhibit the larger relative error as compared to that of u_1. Specifically, Fig. 4.2Evaluation of MLS approximating u_2 (displacement in X_2 direction). (a), (b) and (c) are the plots of $\tilde{\eta}$ versus γ using different interpolation basis. (a): Linear basis. (b): Quadratic basis. (c): Cubic basis. (a), (b) and (c) have the same legend meaning the employed cut-off radius for each MLS interpolation.figure.caption.19a, 4.2Evaluation of MLS approximating u_2 (displacement in X_2 direction). (a), (b) and (c) are the plots of $\tilde{\eta}$ versus γ using different interpolation basis. (a): Linear basis. (b): Quadratic basis. (c): Cubic basis. (a), (b) and (c) have the same legend meaning the employed cut-off radius for each MLS interpolation.figure.caption.19b and 4.2Evaluation of MLS approximating u_2 (displacement in X_2 direction). (a), (b) and (c) are the plots of $\tilde{\eta}$ versus γ using different interpolation basis. (a): Linear basis. (b): Quadratic basis. (c): Cubic basis. (a), (b) and (c) have the same legend meaning the employed cut-off radius for each MLS interpolation.figure.caption.19c show the results for linear basis, quadratic basis and cubic basis, respectively. In each of these plots, the median error $\tilde{\eta}$ is shown as a function of the normalized nearest neighbour distance γ between data points, and each curve represents a cut-off radius r_c.

It is seen that all three subfigures in Fig. 4.2Evaluation of MLS approximating u_2 (displacement in X_2 direction). (a), (b) and (c) are the plots of $\tilde{\eta}$ versus γ using different interpolation basis. (a): Linear basis. (b): Quadratic basis. (c): Cubic basis. (a), (b) and (c) have the same legend meaning the employed cut-off radius for each MLS interpolation.figure.caption.19 showed similar dependence of $\tilde{\eta}$ on γ for $r_c = 0.2$ to 0.5. As γ decreases, which indicates denser distribution of data points, the median error $\tilde{\eta}$ is gradually reduced until $\gamma = 0.0198$. After that $\tilde{\eta}$ appears to converge for sufficiently small γ. This result implies that denser data points in general can improve the accuracy of MLS until a plateau is reached. However,

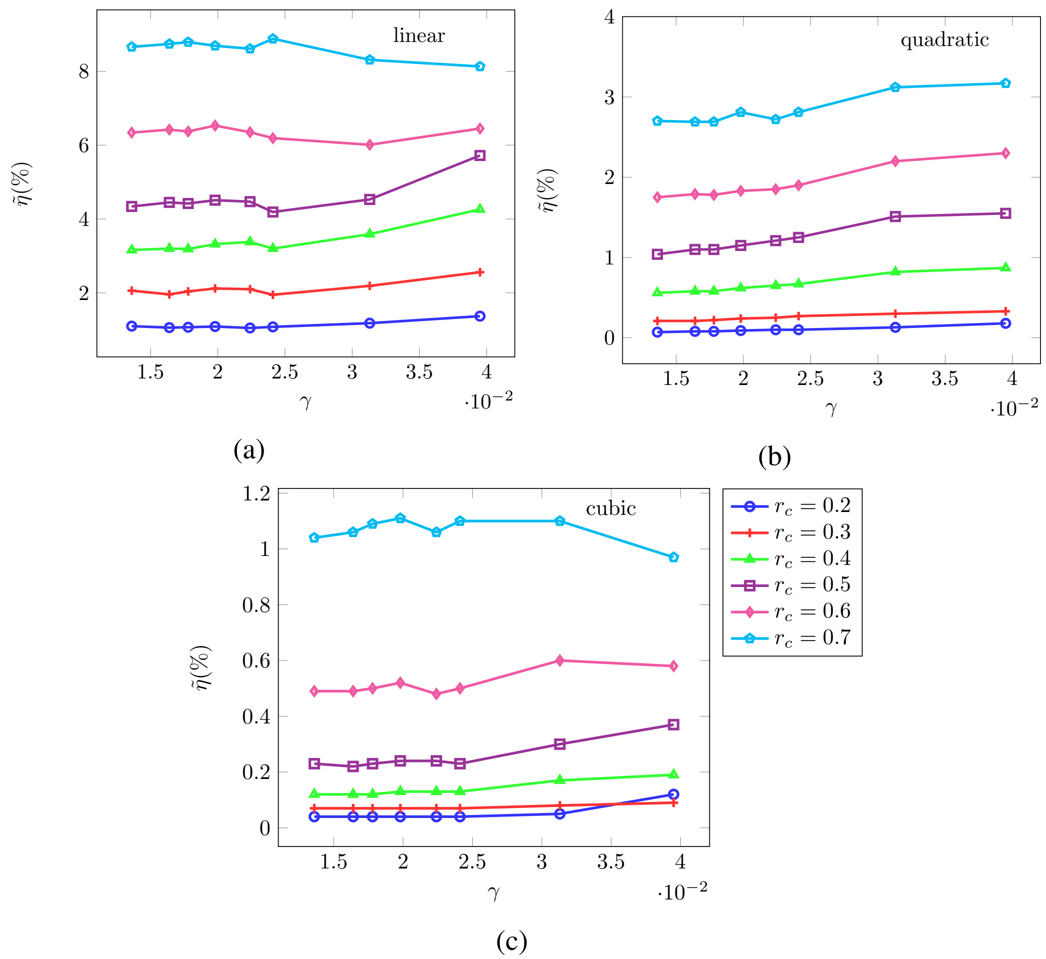

Fig. 4.2. Evaluation of MLS approximating u_2 (displacement in X_2 direction). (a), (b) and (c) are the plots of $\tilde{\eta}$ versus γ using different interpolation basis. (a): Linear basis. (b): Quadratic basis. (c): Cubic basis. (a), (b) and (c) have the same legend meaning the employed cut-off radius for each MLS interpolation.

it should be emphasized that the effect of γ is relatively weak as compared to that of the cut-off radius r_c and the interpolation basis. For example, for the case of $r_c = 0.5$ and cubic basis, the median error $\tilde{\eta}$ is reduced from 0.37% to 0.22% as γ is decreased from 0.0395 to 0.0136.

It is interesting to note that for the two cases of $r_c = 0.6$ and $r_c = 0.7$, the median error $\tilde{\eta}$ may increase with smaller γ (see Fig. 4.2Evaluation of MLS approximating u_2 (displacement in X_2 direction). (a), (b) and (c) are the plots of $\tilde{\eta}$ versus γ using different interpolation basis. (a): Linear basis. (b): Quadratic basis. (c): Cubic basis. (a), (b) and (c) have the same legend meaning the employed cut-off radius for each MLS interpolation.figure.caption.19a and Fig. 4.2Evaluation of MLS approximating u_2 (displacement in X_2 direction). (a), (b) and (c) are the plots of $\tilde{\eta}$ versus γ using different interpolation basis. (a): Linear basis. (b): Quadratic basis. (c): Cubic basis. (a), (b) and (c) have the same legend meaning the employed cut-off radius for each MLS interpolation.figure.caption.19c). This is opposite to the general trend observed for other cases. For example, for $r_c = 0.7$ with linear and cubic basis, the minimum of $\tilde{\eta}$ occurs at $\gamma = 0.0395$ which is the case with the least data points. This is because with larger cut-off radius r_c, more data points are included in the MLS interpolation due to larger region Ω_b (see Fig. 2.1Schematic diagram to demonstrate the weight of data points. In domain Ω (the purple square), A is a point whose displacement we are interested in. B_1, B_2 and B_3 are the data points near A. The yellow circle Ω_b centered at X differentiates the weight of data points. Only data points inside Ω_b contribute to the interpolation.figure.caption.9). If the density of data points is also high, the large number of data points may distort the interpolation formulation as shown in Section 2.1Basic principlesection.2.1, and thus reduce the accuracy.

As for the interpolation basis, a comparison of Fig. 4.2Evaluation of MLS approximating u_2 (displacement in X_2 direction). (a), (b) and (c) are the plots of $\tilde{\eta}$ versus γ using different interpolation basis. (a): Linear basis. (b): Quadratic basis. (c): Cubic basis. (a), (b) and (c) have the same legend meaning the employed cut-off radius for each MLS interpolation.figure.caption.19a, 4.2Evaluation of MLS approximating u_2 (displacement in X_2 direction). (a), (b) and (c) are the plots of $\tilde{\eta}$ versus γ using different interpolation basis. (a): Linear basis. (b): Quadratic basis. (c): Cubic basis. (a), (b) and (c) have the same legend meaning the employed cut-off radius for each MLS interpolation.figure.caption.19b and 4.2Evaluation of MLS approximating u_2 (displacement in X_2 direction). (a), (b) and (c) are the plots of $\tilde{\eta}$ versus γ using different interpolation basis. (a): Linear basis. (b): Quadratic basis. (c): Cubic basis. (a), (b) and (c) have the same legend meaning the employed cut-off radius for each MLS interpolation.figure.caption.19c shows that for linear, quadratic and cubic bases, the median error $\tilde{\eta}$ falls in the range of 1% to 9%, 0.1% to 3.5% and 0.1% to 1.1%, respectively. This means that the cubic basis leads to more accurate interpolation results, which is consistent with our expectation.

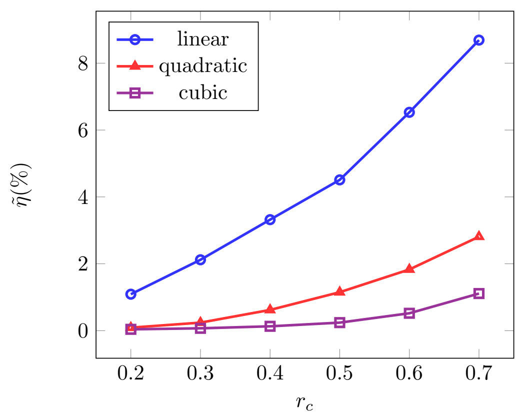

Fig. 4.3. Evaluation of MLS approximating u_2 (displacement in X_2 direction). $\tilde{\eta}$ versus cut-off radius r_c when $\gamma = 0.0198$, namely 800 data points. The legend represents the interpolation basis used for each MLS trial.

Finally, we consider the effect of the cut-off radius r_c, which appears to have a significant impact on the median error $\tilde{\eta}$ as shown in Fig. 4.2Evaluation of MLS approximating u_2 (displacement in X_2 direction). (a), (b) and (c) are the plots of $\tilde{\eta}$ versus γ using different interpolation basis. (a): Linear basis. (b): Quadratic basis. (c): Cubic basis. (a), (b) and (c) have the same legend meaning the employed cut-off radius for each MLS interpolation.figure.caption.19. Since the median error $\tilde{\eta}$ converges when γ decreases to 0.0198, we choose $\gamma = 0.0198$ and collected the data of $\tilde{\eta}$ obtained from different interpolation bases and cut-off radius. Fig. 4.3Evaluation of MLS approximating u_2 (displacement in X_2 direction). $\tilde{\eta}$ versus cut-off radius r_c when $\gamma = 0.0198$, namely 800 data points. The legend represents the interpolation basis used for each MLS trial.figure.caption.20 plots $\tilde{\eta}$ versus cut-off radius r_c at $\gamma = 0.0198$. The three curves represent the results using linear, quadratic and cubic basis, respectively. Fig. 4.3Evaluation of MLS approximating u_2 (displacement in X_2 direction). $\tilde{\eta}$ versus cut-off radius r_c when $\gamma = 0.0198$, namely 800 data points. The legend represents the interpolation basis used for each MLS trial.figure.caption.20 shows that the median error $\tilde{\eta}$ is significantly reduced when r_c decreases from 0.7 to 0.2. In addition, with a proper choice of the cut-off radius r_c (e.g. $r_c < 0.5$), the linear basis is sufficient to keep the median error $\tilde{\eta}$ below 5%. The advantage of using linear basis is the reduced computational cost for interpolation. If higher accuracy is required, quadratic or cubic basis should be used.

4.2 Strain field

Here we consider the accuracy of strain fields computed using MLS method. It was discussed in Section 3.2.2Material propertiessubsection.3.2.2 that for the indentation depth ($\delta = 0.2532h$) we used in the FEA model, effect of large deformation is not negligible. In case of large deformation, there are multiple measures of strain, e.g. the Green strain (see Eq. 2.10Displacement, strain and stress fieldsequation.2.2.10) and true strain (see Eq. 2.18Displacement, strain and stress fieldsequation.2.2.18). Since the strain output from FEA is true strain, we decide to calculate true strain from MLS to evaluate its accuracy. Besides, to highlight the difference between strain measures, we calculate the Green strain and true strain using the displacement field interpolated from MLS method and following

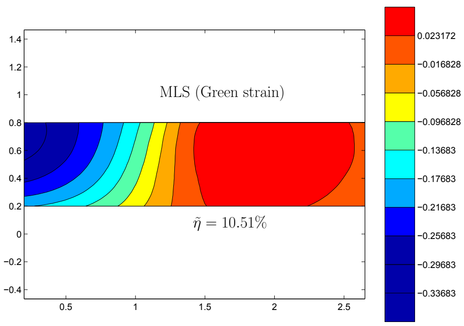

(a)

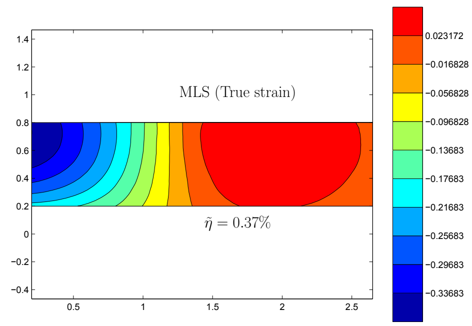

(b)

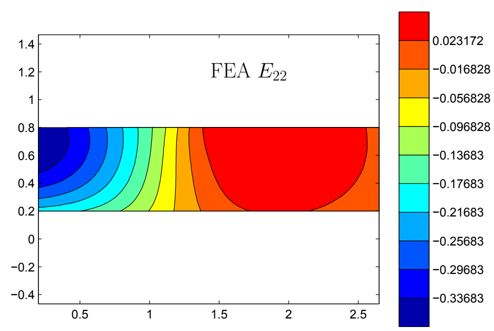

(c)

Fig. 4.4. Strain fields of zone of interest from FEA and MLS. (a): contour plots of strain field ε_{22} from MLS. The strain is calculated from Green strain formula. (b): contour plots of strain field E_{22} from MLS. The strain is calculated from true strain formula. (c): contour plots of strain field E_{22} from FEA. The strain output in ABAQUS is logarithmic strain, namely true strain. $\tilde{\eta}$ is the median of relative errors defined in Eq. 3.13Evaluation of the accuracy of MLS interpolationequation.3.4.13.

Eq. 2.10Displacement, strain and stress fieldsequation.2.2.10a and Eq. 2.18Displacement, strain and stress fieldsequation.2.2.18, respectively. The parameters for MLS method are the same for computing Green strain and true strain: $\gamma = 0.0164$ (1200 data points), cubic basis and $r_c = 0.4$. Fig. 4.4afigure.caption.21 and Fig. 4.4bfigure.caption.21 are respectively the contour plots of the Green strain component ε_{22} and the true strain component E_{22} evaluated from MLS. Compared with the true strain field E_{22} obtained from FEA results as shown in Fig. 4.4cfigure.caption.21, it is obvious that the strain field shown in Fig. 4.4bfigure.caption.21 resembles more with the FEA result. Specifically, the median error $\tilde{\eta}$ for the field in Fig. 4.4bfigure.caption.21 is 0.37%, much smaller than that $\tilde{\eta} = 10.51\%$ for Fig. 4.4afigure.caption.21. Therefore, in the following we use true strain (Eq. 2.18Displacement, strain and stress fieldsequation.2.2.18) in the comparison between MLS and FEA results.

An example of the true strain components E_{11}, E_{12} and E_{22} computed from MLS method together with the corresponding FEA results are present in Fig. 4.5Strain fields of zone of interest from FEA and MLS. (a), (c) and (e): contour plots of strain fields E_{11}, E_{12} and E_{22} from FEA. (b), (d) and (f): contour plots of strain fields E_{11}, E_{12} and E_{22} from MLS. $\tilde{\eta}$ is the median of relative errors defined in Eq. 3.13Evaluation of the accuracy of MLS interpolationequation.3.4.13.figure.caption.22. The parameters used for MLS have been listed in the previous paragraph. From the comparison, it is clear that the MLS method can also accurately reproduce the strain fields. The median error $\tilde{\eta}$ is below 0.5% for all three strain components. This is remarkable given the fact that the strain fields is calculated from the gradient of the interpolated displacement field.

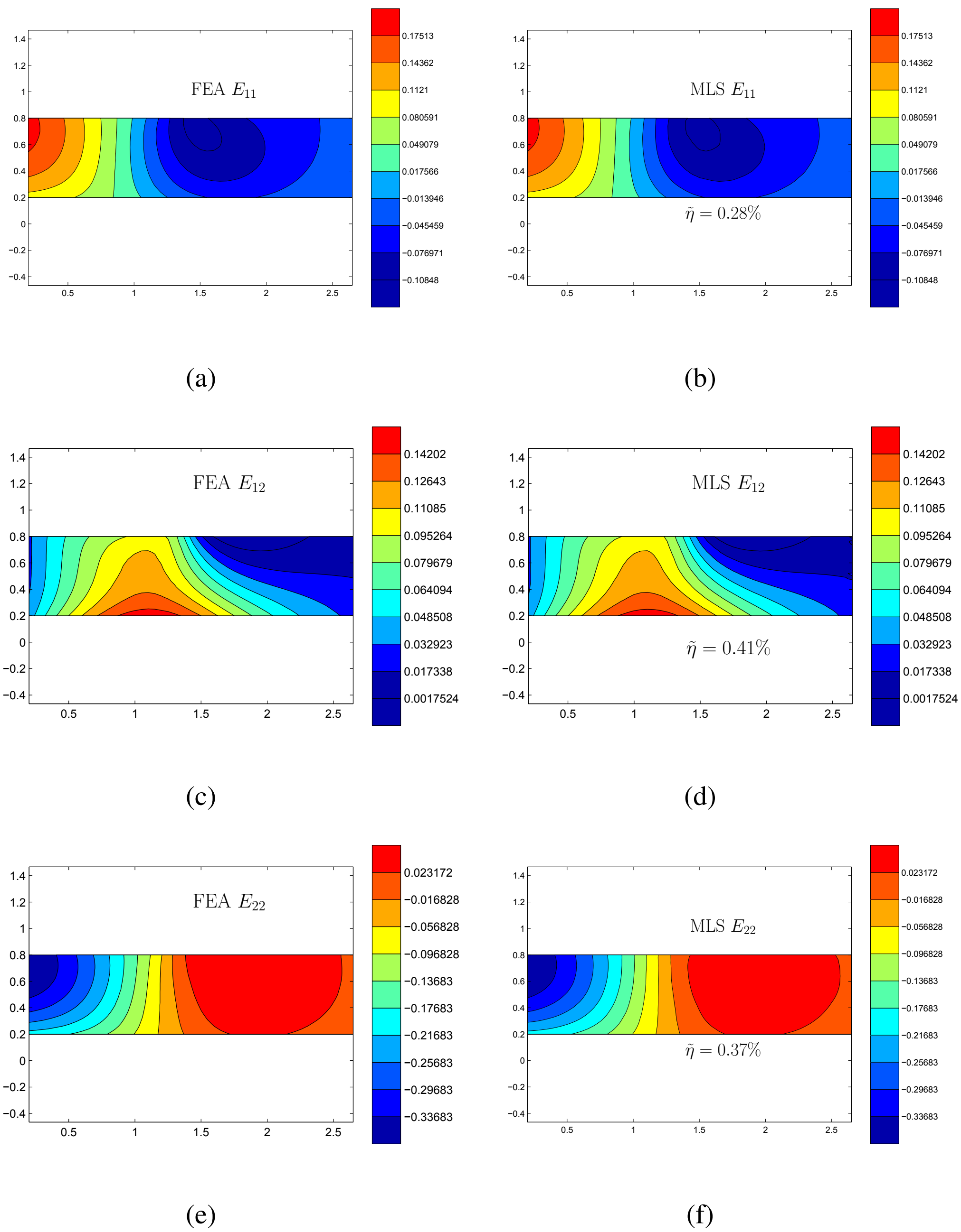

Fig. 4.5. Strain fields of zone of interest from FEA and MLS. (a), (c) and (e): contour plots of strain fields E_{11}, E_{12} and E_{22} from FEA. (b), (d) and (f): contour plots of strain fields E_{11}, E_{12} and E_{22} from MLS. $\tilde{\eta}$ is the median of relative errors defined in Eq. 3.13Evaluation of the accuracy of MLS interpolationequation.3.4.13.

To further evaluate the effects of MLS parameters on the accuracy of the computed strain fields, we calculated the median error $\tilde{\eta}$ of every combinations of parameters listed in Table. 3.2Parameters used in MLS interpolation and zone of interest for each model.table.caption.16. Here we use the strain component E_{22} for the evaluation of $\tilde{\eta}$. Overall the $\tilde{\eta}$ for strain in Fig. 4.6Evaluation of MLS approximating E_{22}. (a), (b) and (c) are the plots of $\tilde{\eta}$ versus γ using different interpolation basis. (a): Linear basis. (b): Quadratic basis. (c): Cubic basis. (a), (b) and (c) have the same legend meaning the employed cut-off radius for each MLS interpolation.figure.caption.23 are larger than those for displacement shown in Fig. 4.2Evaluation of MLS approximating u_2 (displacement in X_2 direction). (a), (b) and (c) are the plots of $\tilde{\eta}$ versus γ using different interpolation basis. (a): Linear basis. (b): Quadratic basis. (c): Cubic basis. (a), (b) and (c) have the same legend meaning the employed cut-off radius for each MLS interpolation.figure.caption.19. This is expected since the strain is evaluated based on the gradient of the interpolated displacement (see Eq. 2.18Displacement, strain and stress fieldsequation.2.2.18 and Eq. 2.19Displacement, strain and stress fieldsequation.2.2.19). In addition, the dependence of $\tilde{\eta}$ on γ follows the same trend as that for the displacement which is discussed in Section 4.1Displacement fieldsection.4.1. As for the interpolation basis, similar to the displacement result, the cubic basis still gives the most accurate results.

Fig. 4.6Evaluation of MLS approximating E_{22}. (a), (b) and (c) are the plots of $\tilde{\eta}$ versus γ using different interpolation basis. (a): Linear basis. (b): Quadratic basis. (c): Cubic basis. (a), (b) and (c) have the same legend meaning the employed cut-off radius for each MLS interpolation.figure.caption.23 also reveals that $\tilde{\eta}$ decreases with smaller cut-off radius r_c, except for a special case where $\gamma = 0.0395, r_c = 0.2$ in Fig. 4.6cfigure.caption.23. For the special case, the median error $\tilde{\eta}$ is the largest one in Fig. 4.6Evaluation of MLS approximating E_{22}. (a), (b) and (c) are the plots of $\tilde{\eta}$ versus γ using different interpolation basis. (a): Linear basis. (b): Quadratic basis. (c): Cubic basis. (a), (b) and (c) have the same legend meaning the employed

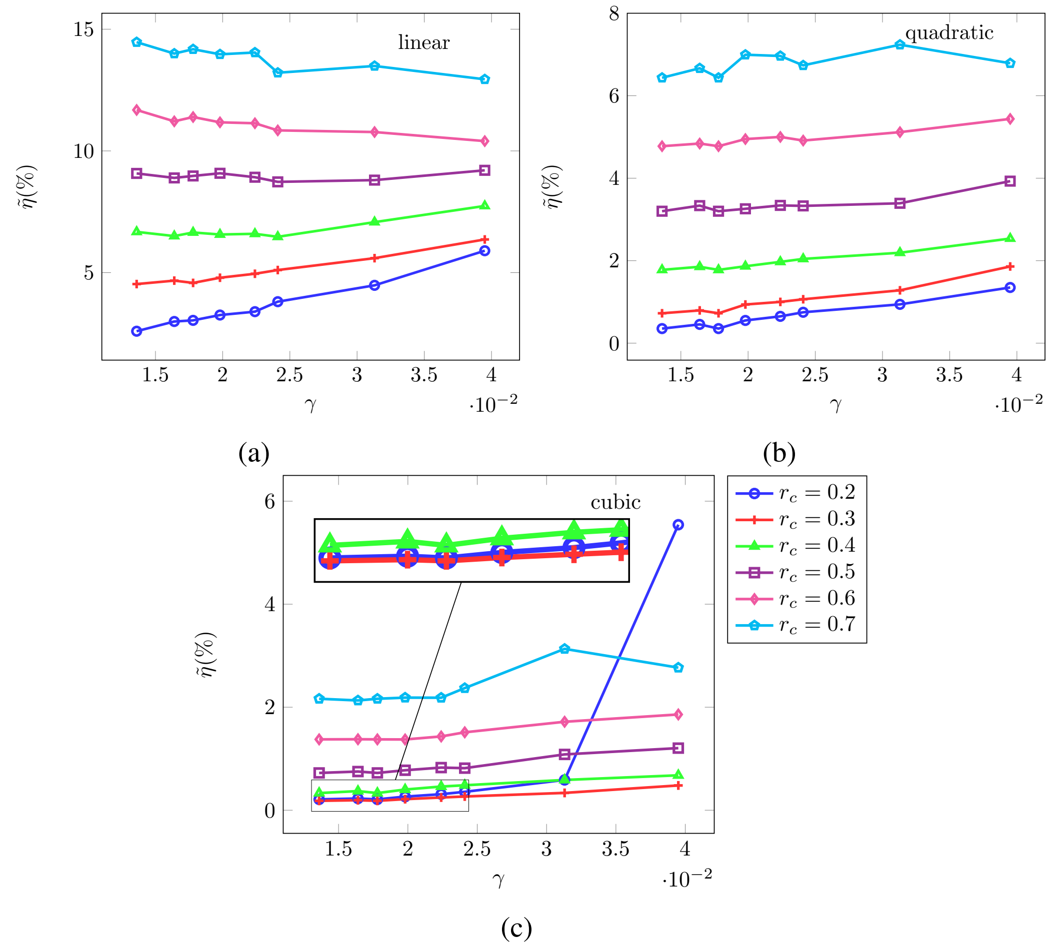

Fig. 4.6. Evaluation of MLS approximating E_{22}. (a), (b) and (c) are the plots of $\tilde{\eta}$ versus γ using different interpolation basis. (a): Linear basis. (b): Quadratic basis. (c): Cubic basis. (a), (b) and (c) have the same legend meaning the employed cut-off radius for each MLS interpolation.

cut-off radius for each MLS interpolation.figure.caption.23c, even higher than most $\tilde{\eta}$ in Fig. 4.6bfigure.caption.23 where quadratic basis was used. This special case clearly does not follow the general trend observed for the dependence of $\tilde{\eta}$ on r_c and interpolation basis. To understand this phenomenon, we note that in this case γ is 0.0395 and there are only 180 data points in the interpolation domain. it is very possible that most data points are excluded by cut-off radius ($r_c = 0.2$). Since the cut-off radius $r_c = 0.2$ is small, it is very possible that there are not enough data points left in the zone Ω_b (see Fig. 2.1Schematic diagram to demonstrate the weight of data points. In domain Ω (the purple square), A is a point whose displacement we are interested in. B_1, B_2 and B_3 are the data points near A. The yellow circle Ω_b centered at X differentiates the weight of data points. Only data points inside Ω_b contribute to the interpolation.figure.caption.9) to accurately determine the coefficients $a(\mathbf{X})$ for the interpolation function. This only occurred for the cubic basis because the length of the coefficient array $a(\mathbf{X})$ is longer than those for linear and quadratic basis so that more data points are required to determiner the coefficients for cubic basis. Similar effect can be observed in the displacement data (see Fig. 4.2Evaluation of MLS approximating u_2 (displacement in X_2 direction). (a), (b) and (c) are the plots of $\tilde{\eta}$ versus γ using different interpolation basis. (a): Linear basis. (b): Quadratic basis. (c): Cubic basis. (a), (b) and (c) have the same legend meaning the employed cut-off radius for each MLS interpolation.figure.caption.19), but it is more dramatic here.

Again, we plot $\tilde{\eta}$ against r_c with γ fixed at 0.0198. The results are shown in Fig. 4.7Plots $\tilde{\eta}$ with cut-off radius r_c at $\gamma = 0.0198$, namely 800 data points. The legend represents the interpolation basis used for each MLS trial.figure.caption.24, and are very similar to the results in Fig. 4.3Evaluation of MLS approximating u_2 (displacement in X_2 direction). $\tilde{\eta}$ versus cut-off radius r_c when $\gamma = 0.0198$, namely 800 data points. The legend represents the interpolation basis used for each MLS trial.figure.caption.20: the median error $\tilde{\eta}$ is significantly reduced for as r_c decreases from 0.7 to 0.2, and the cubic basis performs much better than the linear

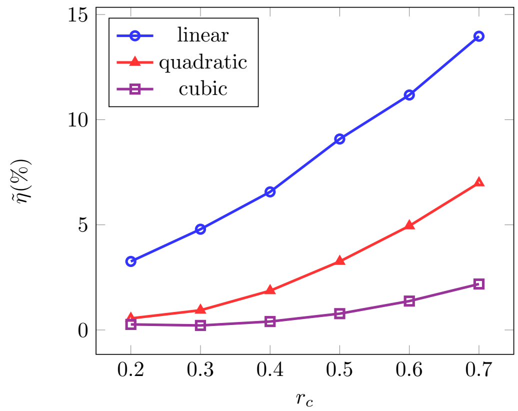

Fig. 4.7. Plots $\tilde{\eta}$ with cut-off radius r_c at $\gamma = 0.0198$, namely 800 data points. The legend represents the interpolation basis used for each MLS trial.

and quadratic basis. If linear basis is used, the median error ranges from 3% to 14%. This means to obtain an curate strain field (e.g. median error $\tilde{\eta} < 5\%$), quadratic and cubic basis should be used for this case.

4.3 Stress field

As discussed in Section 2.2Displacement, strain and stress fieldssection.2.2, a difficulty in calculating the stress field for soft materials, most of which are incompressible, is that there is a hydrostatic pressure term that cannot be determined from the strain or deformation gradient. This problem can be settled, as proposed by Hall et al. [53], by solving it from the equilibrium equation. This results in an integral for the pressure p stated in Eq. 2.28Displacement, strain and stress fieldsequation.2.2.28, which requires the evaluation of the second-order derivative of the displacement (see the laplacian operator in Eq. 2.28Displacement, strain and stress fieldsequation.2.2.28). This places a very stringent requirement for the smoothness and accuracy of the interpolated displacement field. Based on the displacement and strain fields in Section 4.1Displacement fieldsection.4.1 and 4.2Strain fieldsection.4.2, we expect that the pressure term p can not be accurately calculated unless we use cubic basis with a high density of data points. As a result, here for the stress field we will only use cubic basis with $\gamma = 0.0164$ (1200 data points).

Fig. 4.8Stress fields for zone of interest from FEA and MLS. (a), (c) and (e): contour plots of σ_{11}, σ_{12} and σ_{22} from FEA. (b), (d) and (f): contour plots of σ_{11}, σ_{12} and σ_{22} from MLS.figure.caption.25 shows contour plots of the three in-plane Cauchy stress components σ_{11}, σ_{12} and σ_{22} determined from MLS method and the corresponding FEA results. The parameters used for MLS interpolation are $\gamma = 0.0164$ (1200 data points), cubic basis and $r_c = 0.4$. Despite the stringent requirement of calculating the second-order derivative of the displacement, the MLS method still provides accurate results for all three stress components. The median errors $\tilde{\eta}$ for σ_{11}, σ_{12} and σ_{22} are 1.5%, 0.42% and 3.04%, respectively. Note that the error for the shear stress component σ_{12} is much smaller than that of the two normal components. This is because σ_{12} can be directly calculated from the strain field (see Eq. 3.6Expressions of strain and stress componentsequation.3.3.6b) and does not need to hydrostatic pressure term p.

To explore the effect of cut-off radius, in Fig. 4.9Plots $\tilde{\eta}$ versus cut-off radius r_c at $\gamma = 0.0164$, namely 1200 data points. The legend represents the stress components.figure.caption.26 we plot the median error $\tilde{\eta}$ versus r_c using $\gamma = 0.0164$ (1200 data points) and cubic interpolation basis. The three curves represent different stress components. It is seen that for σ_{12} the values of $\tilde{\eta}$ are insensitive to r_c and are all below 5%. The median errors $\tilde{\eta}$ for σ_{11} and σ_{22} are much larger than that of σ_{12} at the same r_c, and can be as high as 20% to 30% for small r_c. As discussed above, σ_{12} can be directly calculated using J and B_{12}, which are determinant of the deformation gradient and a component of left Cauchy green tensor **B**, respectively. The left Cauchy Green deformation tensor **B** represents true strain (see Eq. 2.18Displacement, strain and stress fieldsequation.2.2.18 and Eq. 2.19Displacement, strain and stress fieldsequation.2.2.19) and can be evaluated accurately by the MLS method (see Fig. 4.6Evaluation of MLS approximating E_{22}. (a), (b) and (c) are the plots of $\tilde{\eta}$ versus γ using different interpolation basis. (a): Linear basis.

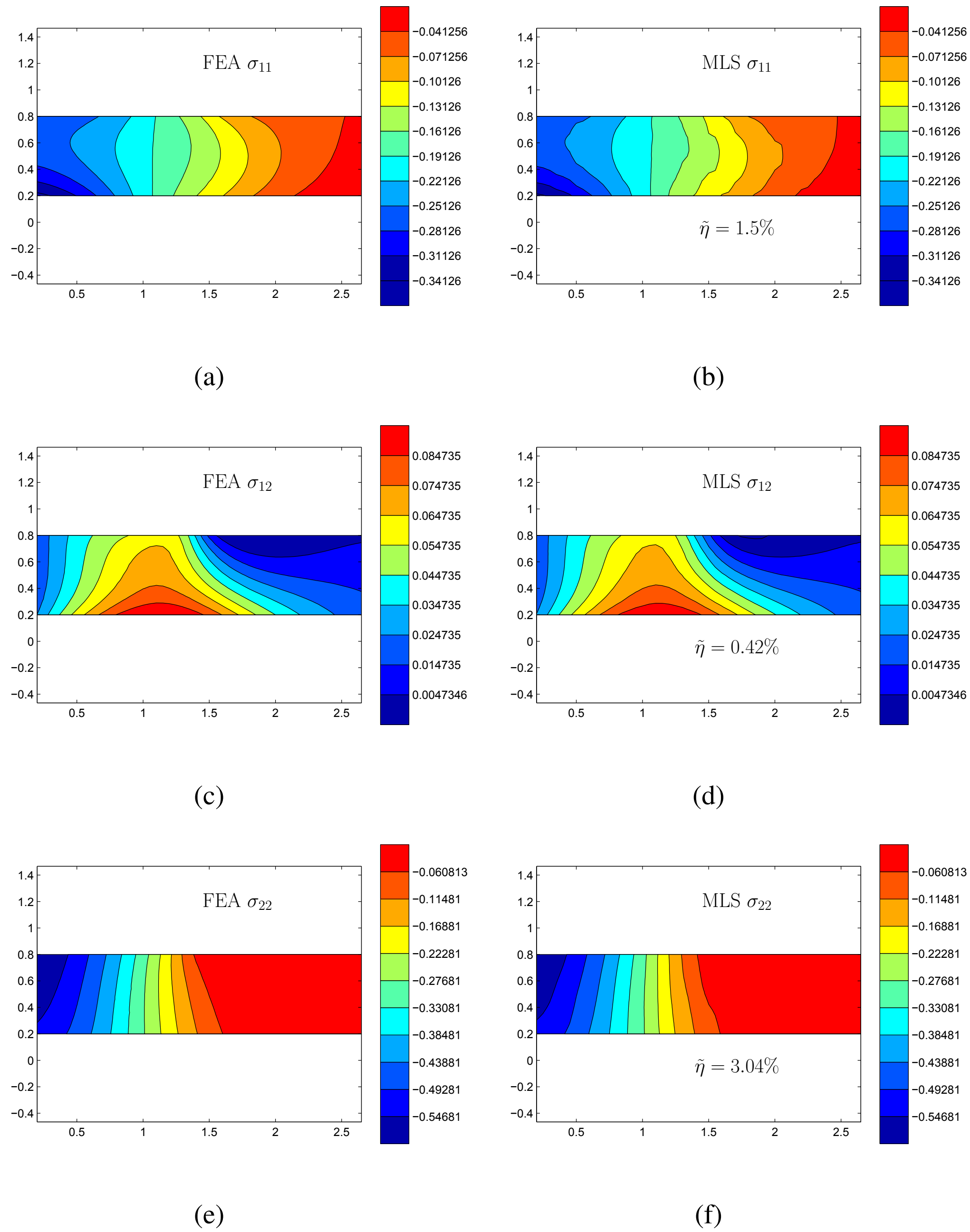

Fig. 4.8. Stress fields for zone of interest from FEA and MLS. (a), (c) and (e): contour plots of σ_{11}, σ_{12} and σ_{22} from FEA. (b), (d) and (f): contour plots of σ_{11}, σ_{12} and σ_{22} from MLS.

(b): Quadratic basis. (c): Cubic basis. (a), (b) and (c) have the same legend meaning the employed cut-off radius for each MLS interpolation.figure.caption.23). The determinant J should be exactly 1 since we used the incompressible neo-Hookean model in the FEA calculation. Due to numerical errors, the J recovered from MLS method is not 1 but very close to 1 (within 2%), as shown in the contour plot of J in Fig. 4.10Contour of J.figure.caption.27. Since it involves integrating and Laplacian operator (Eq. 2.28Displacement, strain and stress fieldsequation.2.2.28), it can be concluded that the errors in σ_{11} and σ_{22} mainly come from the calculation of the hydrostatic pressure term p.

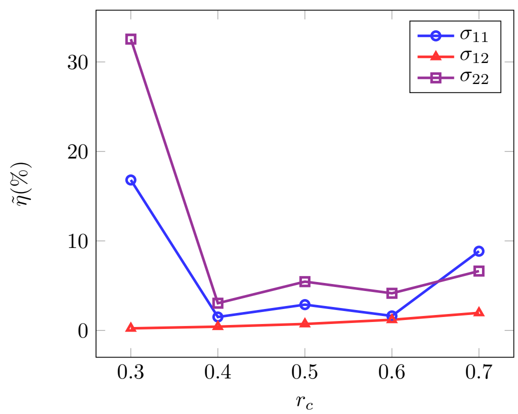

Fig. 4.9. Plots $\tilde{\eta}$ versus cut-off radius r_c at $\gamma = 0.0164$, namely 1200 data points. The legend represents the stress components.

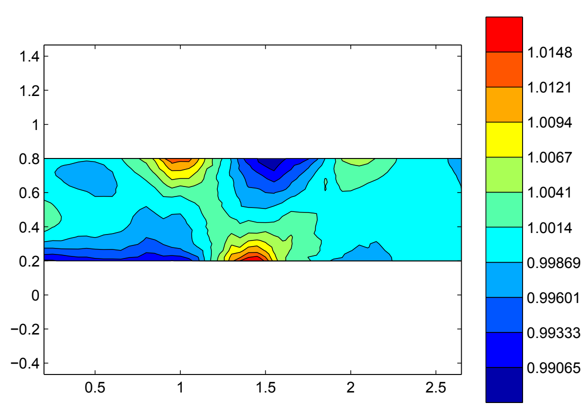

Fig. 4.10. Contour of J.

It should be pointed out that in Fig. 4.9Plots $\tilde{\eta}$ versus cut-off radius r_c at $\gamma = 0.0164$, namely 1200 data points. The legend represents the stress components.figure.caption.26 the median error $\tilde{\eta}$ for σ_{11} and σ_{22} are quite large (20% to 30%) at $r_c = 0.3$. This is because for this relatively small cut-off radius, there may not be enough data points included to accurately calculate the second-order derivative of the displacement field and thus the hydrostatic pressure term p. In fact, we found that for a even smaller cut-off radius $r_c = 0.2$, the second-order derivative of displacement cannot be determined at all due to the lack of data points. This is in contrast to the displacement and strain results where $r_c = 0.2$ usually gives the most accurate results at given γ and interpolation basis.

4.4 Effect of weight function

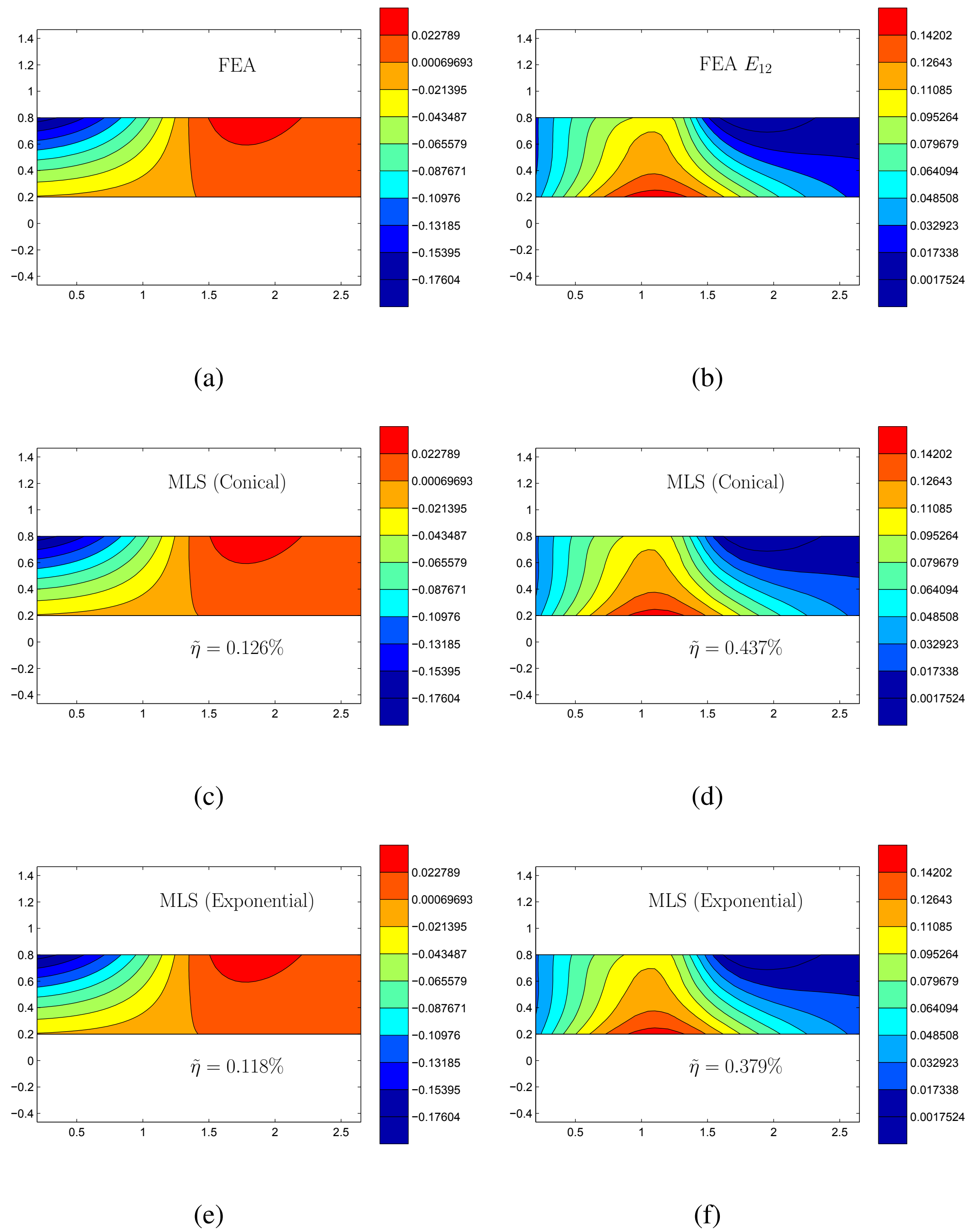

Fig. 4.11. Continuous deformation fields of zone of interest from FEA and MLS. (a),(c) and (e): contour plots of the continuous displacement field u_2 from FEA, MLS (conical weight function) and MLS (exponential weight function). (b),(d) and (f): contour plots of the continuous strain field E_{12} from FEA, MLS (conical weight function) and MLS (exponential weight function).

For all the results shown above, we have only used the conical weight function for MLS interpolation. Here we briefly discuss the effect of weight function by comparing the results with conical and exponential weight function (see Eq. 2.36Parametersequation.2.3.36). Fig. 4.11Continuous deformation fields of zone of interest from FEA and MLS. (a),(c) and (e): contour plots of the continuous displacement field u_2 from FEA, MLS (conical weight function) and MLS (exponential weight function). (b),(d) and (f): contour plots of the continuous strain field E_{12} from FEA, MLS (conical weight function) and MLS (exponential weight function). figure.caption.28 shows the contour plots of displacement component u_2 and the true strain component E_{12} obtained from FEA results as well as MLS method using conical and exponential weight functions. The other parameters used in MLS are $\gamma = 0.0198$ (800 data points), cubic interpolation basis and cut-off radius $r_c = 0.4$.

The three displacement contour plots are shown in Fig. 4.11Continuous deformation fields of zone of interest from FEA and MLS. (a),(c) and (e): contour plots of the continuous displacement field u_2 from FEA, MLS (conical weight function) and MLS (exponential weight function). (b),(d) and (f): contour plots of the continuous strain field E_{12} from FEA, MLS (conical weight function) and MLS (exponential weight function). figure.caption.28a, 4.11Continuous deformation fields of zone of interest from FEA and MLS. (a),(c) and (e): contour plots of the continuous displacement field u_2 from FEA, MLS (conical weight function) and MLS (exponential weight function). (b),(d) and (f): contour plots of the continuous strain field E_{12} from FEA, MLS (conical weight function) and MLS (exponential weight function). figure.caption.28c and 4.11Continuous deformation fields of zone of interest from FEA and MLS. (a),(c) and (e): contour plots of the continuous displacement field u_2 from FEA, MLS (conical weight function) and MLS (exponential weight function). (b),(d) and (f): contour plots of the continuous strain field E_{12} from FEA, MLS (conical weight function) and MLS (exponential weight function). figure.caption.28d. The median error $\tilde{\eta}$ was found to be 0.126% and 0.118% for conical and exponential weight function, respectively. For the strain component E_{12}, the three contour plots are also very close to each other. The median error for conical and exponential weight functions are almost the same: 0.437% and 0.379%, respectively. These results indicate that the MLS interpolation may not be sensitive to the detailed form of the weight function as long as it is a decaying function with the distance from the interpolation point. Of course, a more parametric study is needed for a conclusive understanding of the effect of the weight function, which is a subject of future work.

4.5 Conclusions

In this chapter, we used the indentation model as an example to explore the effect of parameters on the accuracy of MLS interpolation of displacement, strain and stress fields. Results presented in this chapter lead to the following qualitative guideline regarding the selection of parameters for the MLS method.

1. Cubic interpolation basis provides the most accurate measurement among the three interpolation bases. Specifically, for displacement field, linear basis with a proper cut-off radius can yield reasonably accurate results with median relative error $\tilde{\eta}$ below 5%, However, for strain and stress where the first and second-order derivatives of displacement are required, cubic basis is necessary to ensure the accuracy and smoothness of the interpolated field. Based on this observation, it is expected that higher order polynomial basis (e.g. forth order) can further improve the interpolation accuracy, especially for strain and stress fields, but this would also greatly increase the complexity of the interpolation scheme and computational cost.

2. The median error $\tilde{\eta}$ tends to reduce as the data points become denser and converge when the density of data points reaches a critical value. For the indentation example, the median relative error converges when $\gamma = 0.0198$ for displacement. Although this critical value is calculated for a special case, it can still be used to obtain a rough estimate on the density of data points for general applications. It

should be noted that for the computation of stress fields, a higher density is needed for the calculation of the second-order derivative of the displacement field.

3. The cut-off radius r_c is an important parameter that can significantly affect the accuracy of the MLS interpolated results. In general, r_c can neither be too large nor too small for optimized performance of the MLS method. An overly large r_c leads to the inclusion of data points far away from the interpolation point, which weakens the “local interpolation" characteristics of the MLS method and can reduce the accuracy as shown in Fig. 4.2Evaluation of MLS approximating u_2 (displacement in X_2 direction). (a), (b) and (c) are the plots of $\tilde{\eta}$ versus γ using different interpolation basis. (a): Linear basis. (b): Quadratic basis. (c): Cubic basis. (a), (b) and (c) have the same legend meaning the employed cut-off radius for each MLS interpolation.figure.caption.19 (displacement u_2) and Fig. 4.6Evaluation of MLS approximating E_{22}. (a), (b) and (c) are the plots of $\tilde{\eta}$ versus γ using different interpolation basis. (a): Linear basis. (b): Quadratic basis. (c): Cubic basis. (a), (b) and (c) have the same legend meaning the employed cut-off radius for each MLS interpolation.figure.caption.23 (strain E_{22}). An overly small r_c may result in insufficient data points which can reduce the accuracy as well, especially for the stress fields where the second-order derivative of displacement is needed. We expect that the optimal r_c for displacement and strain can also apply to different material constitutive models since the MLS interpolation scheme and the strain in Eq. 2.18Displacement, strain and stress fieldsequation.2.2.18 are independent of the material model. However, for the stress, the optimal r_c may depend on the material model which affects the constitutive equations for stress. Besides, selection of a proper r_c also depends on the density of data points. If the data points are densely distributed, a smaller r_c should be used and vice versa. The principle is to include a certain number of data points that is not too large or too small.

4. The main source of error for computing stress comes from the hydrostatic pressure term p which requires the second-order derivative of the displacement.

For this reason, the median error $\tilde{\eta}$ for shear stress, which does not include p, is much smaller than those for the normal stress components. This difficulty is only present if the material is incompressible or nearly incompressible, and is likely to be a major challenge for soft elastomers and gels which are mostly incompressible.

5. From the two examples shown in Section. 4.4Effect of weight functionsection.4.4, we found that the displacement and strain results are not sensitive to the weight functions. This remains to be confirmed with more extensive parametric studies.

Chapter 5

Application cases with stress concentration

In Chapter 4Results for the indentation example and parametric studychapter.4, we used the indentation model to evaluate the accuracy of the MLS method in mapping the displacement, strain and stress fields and studied the effects of parameters. The results show that the MLS method is capable of accurately mapping the continuous deformation and stress fields from a set of discrete data points if proper parameters are used. These parameters include density of data points (described by the normalized nearest neighbour distance γ), cut-off radius r_c and the interpolation basis. In this chapter, we explore the performance of the MLS method for cases with defects leading to severe stress concentration. To select appropriate parameters for these models, we use results of the parametric study in Chapter 4Results for the indentation example and parametric studychapter.4. First, for interpolation basis, cubic basis will be utilized since it was shown to give the most accurate results, especially for strain and stress fields. Second, for data points, in the previous chapter we found that the median relative error $\tilde{\eta}$ converged when the normalized nearest neighbour distance γ is about 0.0198. This value corresponded to a total number of 800 data points for the indention model. Based on this result, we will used the same number of data points (800) for the two cases considered in this chapter. However, we note that the resulting γ may not be exactly 0.0198 (but still is close to this value) since the data points are randomly selected from nodes of the FEA results. Third, for the cut-off radius r_c, we found that it should neither be too large nor too small. The optimal choice of r_c depends on what quantity, e.g. displacement or stress, is to be calculated. Here we will try different values of r_c for the two new models studied in this chapter. Specifically, r_c for the tension model ranges from 0.6 to 1 while r_c for the crack model covers $[0.003, 0.008]$. Since the zone of interest of the crack model is much smaller than that of the tension model, r_c used for the former is much less than that of the latter. As to the weight function, we will take the conical weight function like what we did in Chapter 4Results for the indentation example and parametric studychapter.4.

5.1 Plate with a hole under tension

5.1.1 Displacement and strain fields

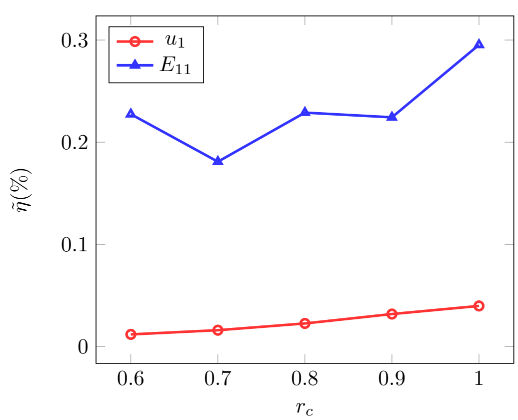

Fig. 5.1. Evaluation of MLS approximating u_1 and E_{11}. Plots $\tilde{\eta}$ with cut-off radius r_c at 800 data points with cubic basis.

A plate with a circular hole is under uni-axial tension as shown in Fig. 3.1bfigure.caption.11. For this model, we applied two different displacements on the plate: $u_1 = 20$ and $u_1 = 40$ (see Table. 3.1Finite element simulation details.table.caption.12). Here we present only the results of $u_1 = 20$ and those for $u_1 = 40$ are included in Appendix

A. As described above, we varied the cut-off radius r_c from 0.6 to 1. The median relative error $\tilde{\eta}$ for the displacement component u_1 and strain component E_{11} are plotted versus r_c in Fig. 5.1Evaluation of MLS approximating u_1 and E_{11}. Plots $\tilde{\eta}$ with cut-off radius r_c at 800 data points with cubic basis.figure.caption.29. The specific displacement and strain components (u_1 and E_{11}) are selected here because the plate is loaded under uni-axial tension along the X_1 direction. For u_1, a clear increasing trend of $\tilde{\eta}$ is shown with increasing r_c. The smallest $\tilde{\eta}$ for u_1 is reached at $r_c = 0.6$. For E_{11}, it appears that $r_c = 0.7$ yields the lowest $\tilde{\eta}$.

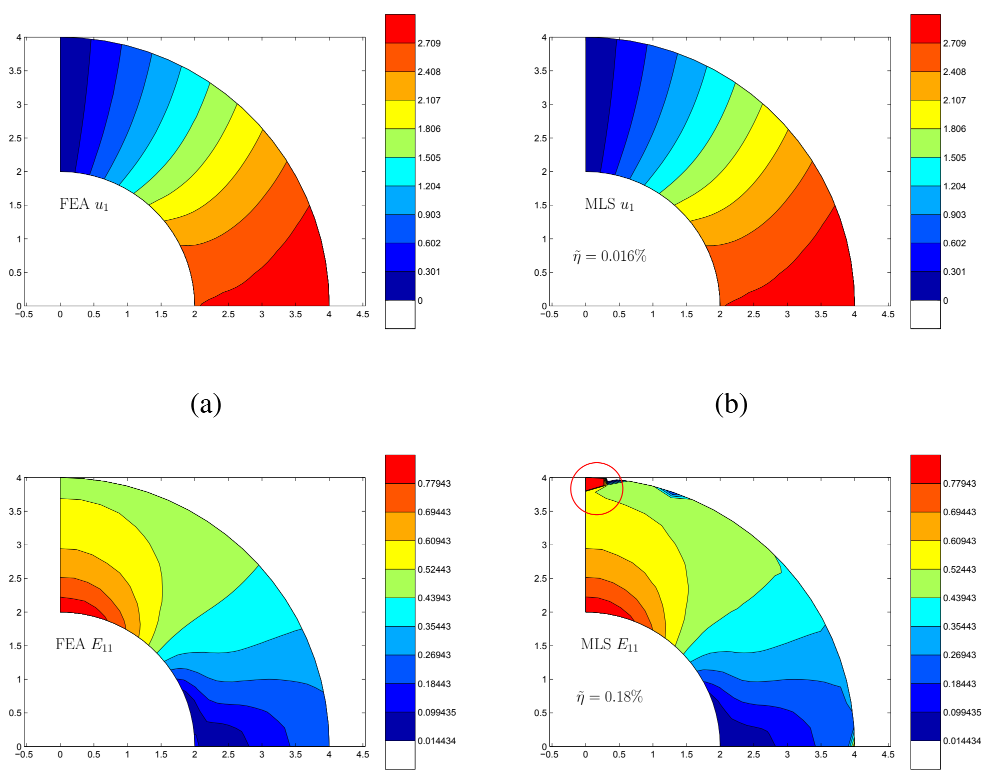

(a) (b)

(c) (d)

Fig. 5.2. Displacement and strain fields for zone of interest from FEA and MLS. (a) and (c) : contour plots of u_1 and E_{11} from FEA. (b) and (d): contour plots of u_1 and E_{11} from MLS.

Based on the results in Fig. 5.1Evaluation of MLS approximating u_1 and E_{11}. Plots $\tilde{\eta}$ with cut-off radius r_c at 800 data points with cubic basis.figure.caption.29, we choose $r_c = 0.7$ and present the contour plots of the displacement component

u_1 and strain component E_{11} in Fig. 5.2Displacement and strain fields for zone of interest from FEA and MLS. (a) and (c) : contour plots of u_1 and E_{11} from FEA. (b) and (d): contour plots of u_1 and E_{11} from MLS.figure.caption.30b and Fig. 5.2Displacement and strain fields for zone of interest from FEA and MLS. (a) and (c) : contour plots of u_1 and E_{11} from FEA. (b) and (d): contour plots of u_1 and E_{11} from MLS.figure.caption.30d. Fig. 5.2afigure.caption.30 and Fig. 5.2cfigure.caption.30 are plotted using corresponding FEA results. Overall, we can see that the displacement and stress fields reproduced from the MLS method are very close to the FEA results. The median relative error $\tilde{\eta}$ was found to be 0.016% and 0.18% for the displacement and strain fields, respectively. Note that, severe discrepancy between the FEA and MLS results in E_{11} is observed in a small area near the top corner of the zone of interest (marked by the red circle in Fig. 5.2dfigure.caption.30). This is attributed to the low density of data points in this region (see Fig. 5.3Stress fields for zone of interest from FEA and MLS. (a): contour plots of σ_{11} from FEA. (b): contour plots of σ_{11} from MLS in method B. (c): contour plots of σ_{11} from MLS in method A. (d): contour plots of σ_{11} from MLS in method A with data points.figure.caption.31d for distribution of the data points).

5.1.2 Stress field

In the indentation model discussed in Chapter 4Results for the indentation example and parametric studychapter.4, we calculated the hydrostatic pressure term p by integrating the second-order derivatives of the displacements (see Eq. 2.28Displacement, strain and stress fieldsequation.2.2.28). However, in this model, plane stress condition is assumed, which implies that the out-of-plane normal stress component σ_{33} is identically zero in the entire zone of interest. As a result, the hydrostatic pressure term p can be alternatively calculated by setting $\sigma_{33} = 0$ in Eq. 2.25Displacement, strain and stress fieldsequation.2.2.25. This method does not require the computation of second-order derivatives of displacement, and thus is expected to give more accurate results for the stress field. To demonstrate this point, here we attempt both methods of calculating the hydrostatic pressure term p: 1) following Eq. 2.28Displacement, strain and stress fieldsequation.2.2.28 to integrate the second-order derivatives of displacement (Method A); 2) directly calculating p by setting $\sigma_{33} = 0$ in Eq. 2.25Displacement, strain and stress fieldsequation.2.2.25 (Method B).

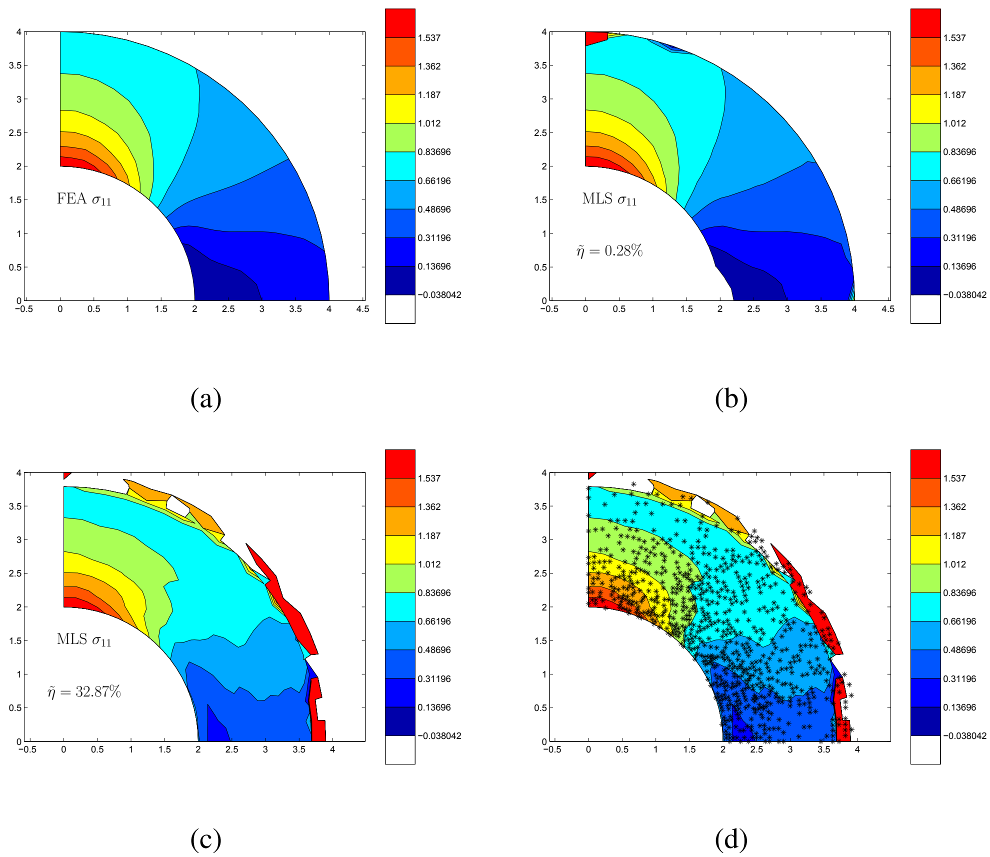

Fig. 5.3. Stress fields for zone of interest from FEA and MLS. (a): contour plots of σ_{11} from FEA. (b): contour plots of σ_{11} from MLS in method B. (c): contour plots of σ_{11} from MLS in method A. (d): contour plots of σ_{11} from MLS in method A with data points.

Fig. 5.3Stress fields for zone of interest from FEA and MLS. (a): contour plots of σ_{11} from FEA. (b): contour plots of σ_{11} from MLS in method B. (c): contour plots of σ_{11} from MLS in method A. (d): contour plots of σ_{11} from MLS in method A with data points.figure.caption.31 shows the contour plots of σ_{11} obtained from multiple sources of data. The benchmark field obtained from FEA results is shown in Fig. 5.3afigure.caption.31. The stress fields reproduced by the MLS method with $r_c = 0.7$, using Method A and Method B for the hydrostatic pressure term p, are shown in Fig. 5.3Stress fields for zone of interest from FEA and MLS. (a): contour plots of σ_{11} from FEA. (b): contour plots of σ_{11} from MLS in method B. (c): contour plots of σ_{11} from MLS in method A. (d): contour plots of σ_{11} from MLS in method A with data points.figure.caption.31c and 5.3Stress fields for zone of interest from FEA and MLS. (a): contour plots of σ_{11} from FEA. (b): contour plots of σ_{11} from MLS in method B. (c): contour plots of σ_{11} from MLS in method A. (d): contour plots of σ_{11} from MLS in method A with data points.figure.caption.31b, respectively. The median relative error $\tilde{\eta}$ is found to be 0.28% when Method B is used, which is much smaller than that ($\tilde{\eta} = 32.87\%$) of Method A. Clearly, Method B gives more accurate results for the stress field by removing the need of calculating the second-order derivative of the displacement field. However, Method B is only valid under plane stress condition. For general three-dimensional deformation, we still need to use Method A for calculating the stress field. It should be noted that the large errors for the results given by Method A mainly occurred in the region surrounding the outer arc. We believe this is due to the lack of data points in this region, which is confirmed in Fig. 5.3dfigure.caption.31 where the distribution of data points is plotted. Denser data points are needed in this region for calculating the second-order derivative of displacement in Method A.

5.2 Two-dimensional crack

5.2.1 Displacement and strain fields

The third model is a two-dimensional edge crack as shown in Fig. 3.1cfigure.caption.11. The stress concentration here is more severe than that of the second model shown in Fig. 3.1bfigure.caption.11. This model is also under the assumption of plane stress (see Table. 3.1Finite element simulation details.table.caption.12). Similar to the previous model, we used two displacement loadings, $u_2 = 5$ and $u_2 = 10$. The results for $u_2 = 5$ are presented here while those for $u_2 = 10$ are included in

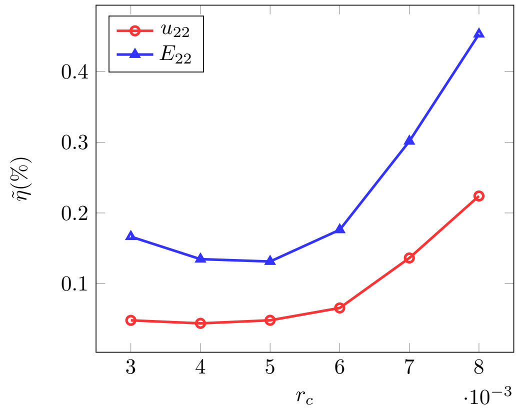

Fig. 5.4. Evaluation of MLS approximating u_2 and E_{22}. Plots $\tilde{\eta}$ with cut-off radius r_c at 800 data points with cubic basis.

Appendix B. We tried a number of cut-off radius r_c ranging form 0.003 to 0.008. The median relative error $\tilde{\eta}$ for the displacement component u_2 and strain component E_{22} for different r_c are shown in Fig. 5.4Evaluation of MLS approximating u_2 and E_{22}. Plots $\tilde{\eta}$ with cut-off radius r_c at 800 data points with cubic basis.figure.caption.32. Since the crack is opening along X_2 direction, we choose to present the results of displacement component u_2 and strain component E_{22}. We can see that at $r_c = 0.005$ $\tilde{\eta}$ reaches minimum for E_{22}. For u_2, $\tilde{\eta}$ converges when r_c is below 0.005. Therefore, we will use $r_c = 0.005$ and show the contour plots of displacement u_2 and true strain E_{22} in the following.

The contour plots of u_2 and E_{22} reproduced using the MLS method are shown in Fig. 5.5bfigure.caption.33 and 5.5dfigure.caption.33, while the corresponding results obtained from FEA are shown in Fig. 5.5afigure.caption.33 and 5.5cfigure.caption.33. The displacement fields illustrated in Fig. 5.5afigure.caption.33 (FEA) and Fig. 5.5bfigure.caption.33 (MLS) are almost identical to each other, except the region directly ahead of the crack tip where $X_1 > 0$ and $X_2 = 0$. For strain E_{22}, the field given by the MLS method faithfully reproduced the rapid decay of strain when moving away from the crack tip. Overall, the displacement and strain fields reproduced

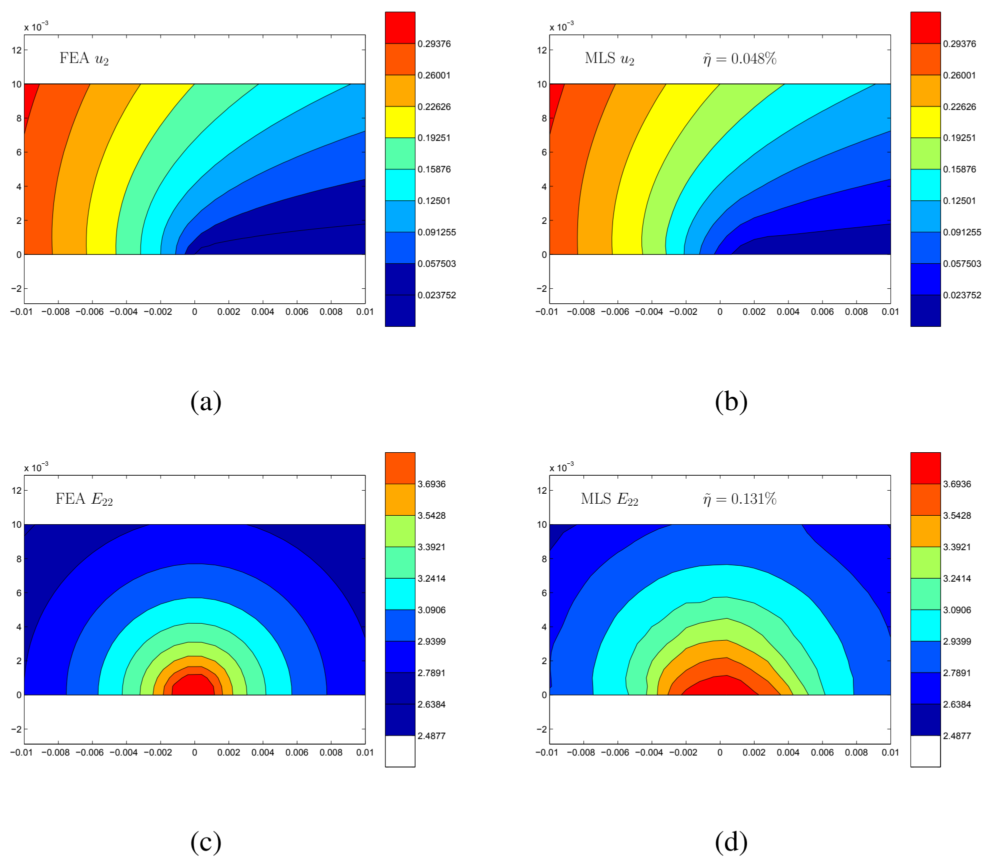

Fig. 5.5. Displacement and strain fields for zone of interest from FEA and MLS. (a) and (c) : contour plots of u_2 and E_{22} from FEA. (b) and (d): contour plots of u_2 and E_{22} from MLS.

using the MLS method agree well with the benchmark FEA results. The median relative errors for the displacement u_2 and strain E_{22} are 0.048% and 0.131%, respectively.

5.2.2 Stress field

In Section 5.1.2Stress fieldsubsection.5.1.2, we have demonstrated the advantage of directly computing the hydrostatic pressure term p in plane stress cases by setting $\sigma_{33} = 0$ in Eq. 2.25Displacement, strain and stress fieldsequation.2.2.25. This method will be adopted here for calculating the stress field in the crack tip region.

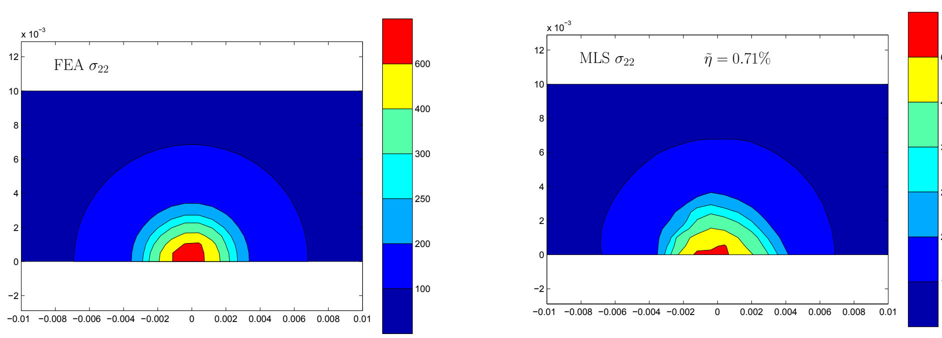

(a)

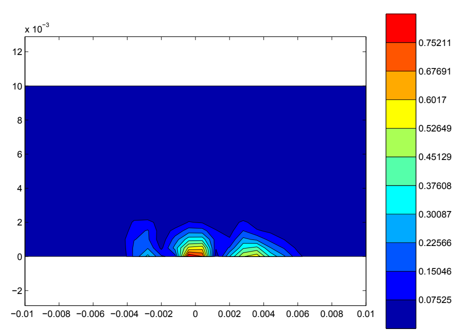

(b)

Fig. 5.6. Stress fields for zone of interest from FEA and MLS. (a): contour plot of σ_{22} from FEA. (b): contour plot of σ_{22} from MLS in method B. (c): contour plot of the relative error η for stress component σ_{22}.

The contours of σ_{22} obtained from FEA results and calculated using MLS method are present in Fig. 5.6Stress fields for zone of interest from FEA and MLS. (a): contour plot of σ_{22} from FEA. (b): contour plot of σ_{22} from MLS in method B. (c): contour plot of the relative error η for stress component σ_{22}. figure.caption.34a and Fig. 5.6Stress fields for zone of interest from FEA and MLS. (a): contour plot of σ_{22} from FEA. (b): contour plot of σ_{22} from MLS in method B. (c): contour plot of the relative error η for stress component σ_{22}. figure.caption.34b. A severe stress concentration can be observed near the crack tip, which makes it difficult to reduce the relative error of the stress field. It can be seen that in Fig. 5.6Stress fields for zone of interest from FEA and MLS. (a): contour plot of σ_{22} from FEA. (b): contour plot of σ_{22} from MLS in method B. (c): contour plot of the relative error η for stress component σ_{22}. figure.caption.34c that large relative errors (larger than 20%) mostly occur very close to the crack tip. The relative error is dramatically reduced below 7% away from the crack tip, and the median relative error $\tilde{\eta}$ was found to be 0.71%. What's more, from the pie chart shown in Fig. 5.7Pie chart of relative errors η.figure.caption.35, we can find that over 85% of relative error η are below 5%. This also supports that the MLS method finished a good mapping of σ_{22}.

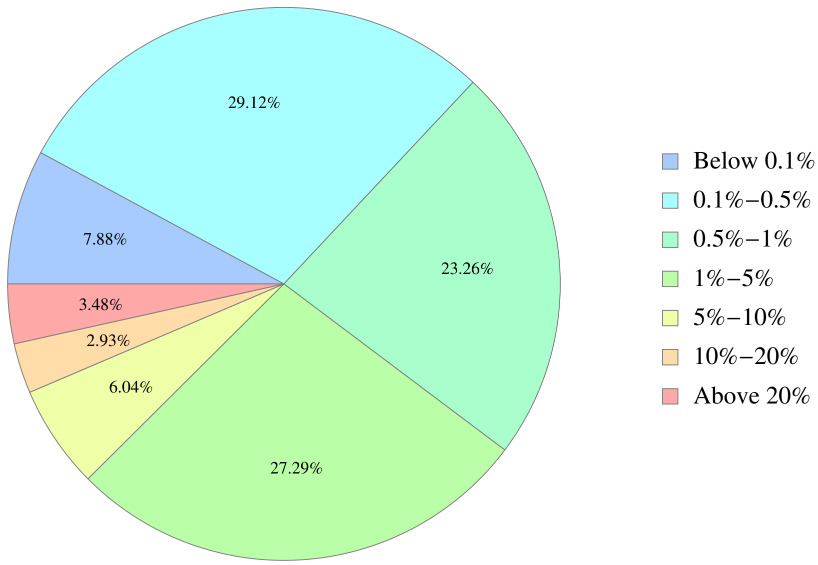

Fig. 5.7. Pie chart of relative errors η.

5.3 Conclusions

In this chapter we studied two models with defects (hole and the crack) which lead to stress concentration. Both models are subjected to large deformation. The results in Section 5.1Plate with a hole under tensionsection.5.1 and Section 5.2Two-dimensional cracksection.5.2 demonstrated that MLS was able to achieve accurate full-field measurement of large deformation and stress concentration when proper parameters were chosen. This chapter mainly discuss how the choice of r_c influences the results. And the optimized values of r_c are 0.7 and 0.005 for the two models.

For these two models, plane stress condition was assumed which greatly simplified the calculation of stress field since the hydrostatic pressure term p can be directly determined from the zero out-of-plane normal stress. This method was also shown to give much more accurate stress field than the method where hydrostatic pressure term p is calculated by integrating the second-order derivative of displacement field. It is noteworthy that this method is only valid for plane stress problems. As to general three-dimensional case, the hydrostatic pressure p still needs to be calculated from the second-order derivative of displacement field following Eq. 2.28Displacement, strain and stress fieldsequation.2.2.28.

Chapter 6

Conclusions and future work

In summary, the goal of this thesis is to understand 1), the accuracy of MLS in mapping deformation and stress fields within soft material; 2) how the parameters of MLS affect the interpolation results; 3) the capability of MLS in measuring cases with large deformation and stress concentration. The first two goals were achieved by examining an indentation model discussed in Chapter 4Results for the indentation example and parametric studychapter.4. Different combinations of parameters were used to calculate the displacement, strain and stress fields inside the soft gel under indentation. By comparing the results from MLS with the benchmark FEA, we obtained the following general qualitative understandings on the effect of parameters. The first one is that cubic interpolation basis acts the best comparing with other two bases used in this work. Next, the interpolation results converge with a sufficiently dense distribution of data points. Thirdly, the cut-off radius can never be too large or too small and in general there exists an optimal cut-off radius to minimize the numerical errors. Finally, the errors of mapping stress fields for incompressible materials, which is the case for most soft elastomers and gels, are mainly from calculating the hydrostatic pressure term p.

Based on the findings from the indentation model, we apply MLS to full-field measurement of two other models with defects and stress concentration. The measured displacement, strain and stress fields agreed well with those from FEA. These two examples demonstrated the capability of MLS to measure nonlinear deformation, especially for cases with high spatial gradients for deformation and stress fields.

Overall our study shows that MLS is a promising method to make full-field measurement within soft material exhibiting large deformation and stress concentration. Looking forward, it can be further improved in the following aspects. First, to reduce the errors for mapping stress fields, the method of calculating the hydrostatic pressure p can be improved. As shown in Eq. 2.28Displacement, strain and stress fieldsequation.2.2.28, p is determined by integrating the second-order derivative of displacement from a point where any one of the normal stress components is given. In principle, the result of p should be independent of the integration path selected, but in reality different integration paths may cause different degree of numerical errors. In this work, we only choose one integration path, but it is also possible to use a large number of integration paths and perform statistical analysis to minimize the error in the hydrostatic pressure p. Besides, since we only choose the data points inside the zone of interest, it is possible that there are insufficient data points near the boundary (see Fig. 3.4cfigure.caption.15). In Chapter 4Results for the indentation example and parametric studychapter.4 and 5Application cases with stress concentrationchapter.5, we have mentioned that insufficient data points may lead to large errors (see Fig. 4.6cfigure.caption.23) and non-smoothness in the interpolated fields (see Fig. 5.3dfigure.caption.31). To avoid this situation, we do not need to choose data points inside the zone of interest but can select a few more data points outside the zone of interest.

Appendix A: Plate under tension (loading 2)

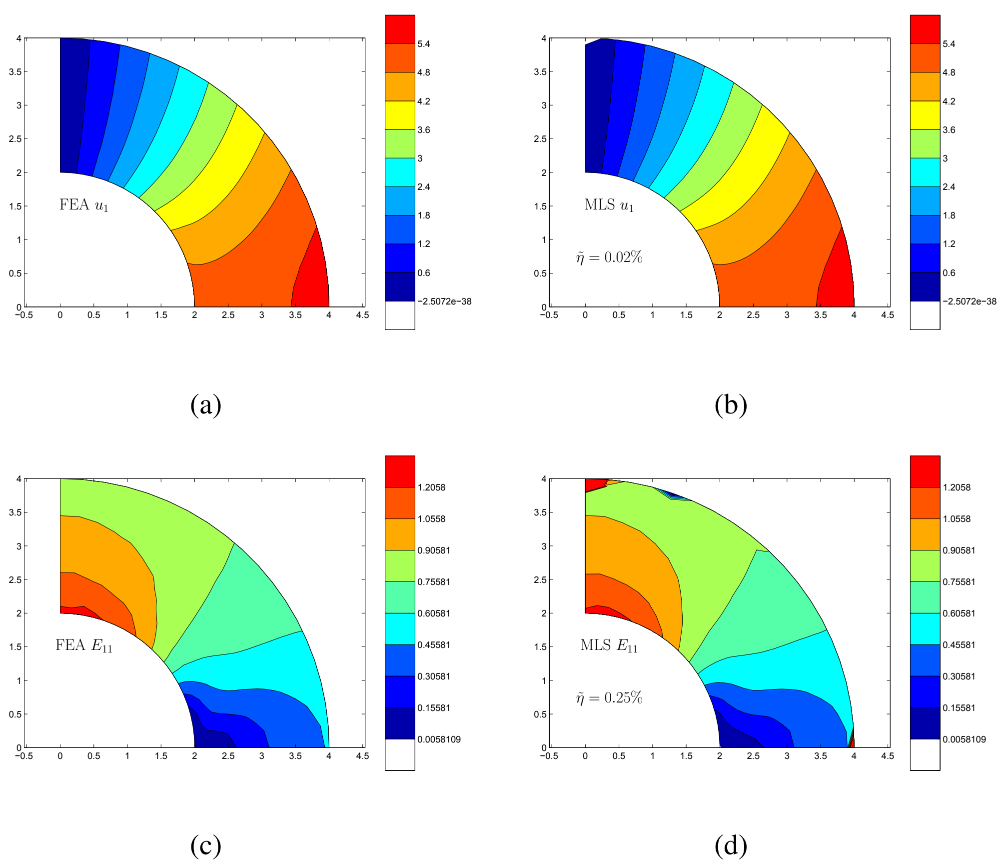

Fig. A1. Displacement and strain fields for zone of interest from FEA and MLS. (a) and (c) : contour plots of u_1 and E_{11} from FEA. (b) and (d): contour plots of u_1 and E_{11} from MLS.

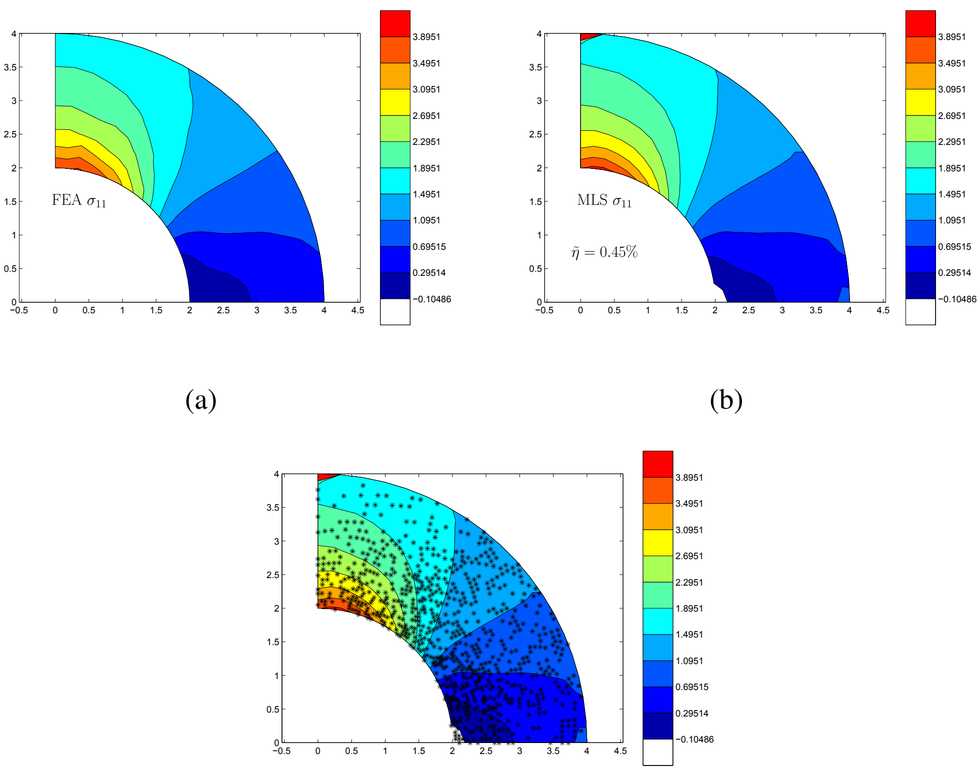

(a)

(b)

(c)

Fig. A2. Stress fields for zone of interest from FEA and MLS. (a): contour plots of σ_{11} from FEA. (b): contour plots of σ_{11} from MLS in method B. (c) contour plots of σ_{11} from MLS in method B with data points.

Appendix B: Two-dimensional crack (loading 2)

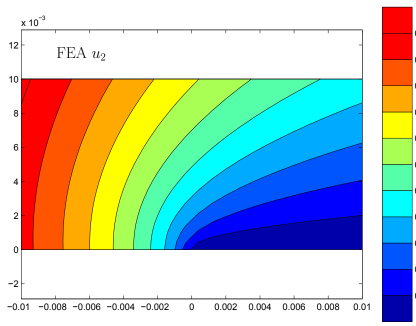

(a)

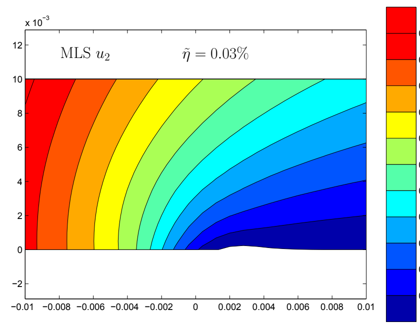

(b)

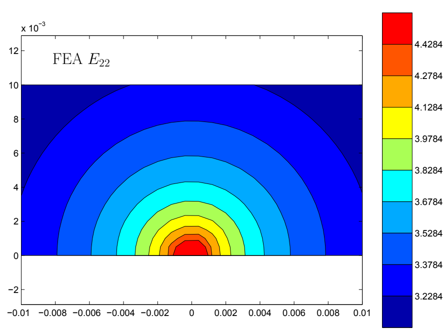

(c)

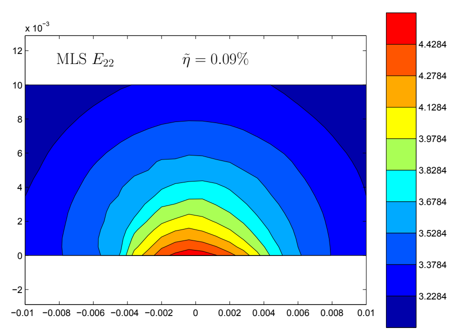

(d)

Fig. B1. Displacement and strain fields for zone of interest from FEA and MLS. (a) and (c) : contour plots of u_2 and E_{22} from FEA. (b) and (d): contour plots of u_2 and E_{22} from MLS.

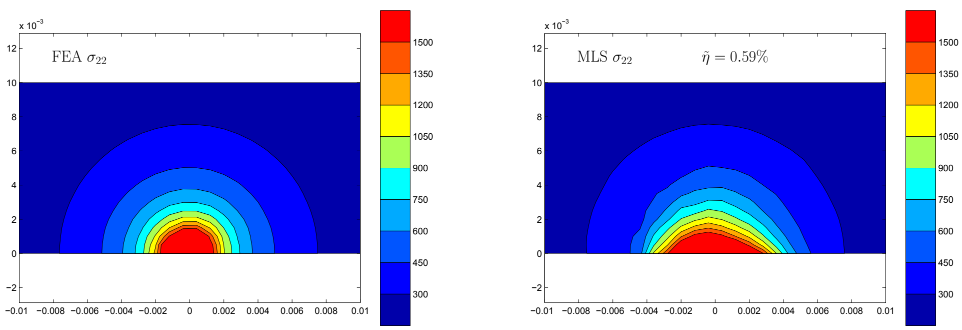

(a) (b)

Fig. B2. Stress fields for zone of interest from FEA and MLS. (a): contour plot of σ_{22} from FEA. (b): contour plot of σ_{22} from MLS in method B. (c): contour plot of the relative error η for stress component σ_{22}.

Bibliography

[1] Bing Pan, Kemao Qian, Huimin Xie, and Anand Asundi. Two-dimensional digital image correlation for in-plane displacement and strain measurement: a review. *Measurement science and technology*, 20(6):062001, 2009.

[2] William N Sharpe Jr and William N Sharpe. *Springer handbook of experimental solid mechanics*. Springer Science & Business Media, 2008.

[3] Cesar A Sciammarella and Federico M Sciammarella. *Experimental mechanics of solids*. John Wiley & Sons, 2012.

[4] Anbo Wang, Shi He, Xiaojan Fang, Xiaodan Jin, and Junxiu Lin. Optical fiber pressure sensor based on photoelasticity and its application. *Lightwave Technology, Journal of*, 10(10):1466–1472, 1992.

[5] Yasunori Nishijima and Gerald Oster. Moiré patterns: Their application to refractive index and refractiveindex gradient measurements. *JOSA*, 54(1):1–4, 1964.

[6] JS Sirkis and TJ Lim. Displacement and strain measurement with automated grid methods. *Experimental Mechanics*, 31(4):382–388, 1991.

[7] AC Thompson, J Llacer, L Campbell Finman, EB Hughes, JN Otis, S Wilson, and HD Zeman. Computed tomography using synchrotron radiation. *Nuclear Instruments and Methods in Physics Research*, 222(1):319–323, 1984.

[8] K Ramesh. Digital photoelasticity, 2000.

[9] K Ramesh, T Kasimayan, and B Neethi Simon. Digital photoelasticity–a comprehensive review. *The Journal of Strain Analysis for Engineering Design*, 46(4):245–266, 2011.

[10] Hans Mueller. The theory of photoelasticity*. *Journal of the American Ceramic Society*, 21(1):27–33, 1938.

[11] Zhaoming Zhu and Thomas G Brown. Stress-induced birefringence in microstructured optical fibers. *Optics letters*, 28(23):2306–2308, 2003.

[12] NM Neves, AS Pouzada, JHD Voerman, and PC Powell. The use of birefringence for predicting the stiffness of injection molded polycarbonate discs. *Polymer Engineering & Science*, 38(10):1770–1777, 1998.

[13] James W Dally and William F Riley. Experimental stress analysis, 1991. *McGraw and Hill, New York*.

[14] G Petrucci. Full-field automatic evaluation of an isoclinic parameter in white light. *Experimental mechanics*, 37(4):420–426, 1997.

[15] MW Hyer and D Liu. Stresses in pin-loaded orthotropic plates: photoelastic results. *Journal of composite materials*, 19(2):138–153, 1985.

[16] GM Brown and JL Sullivan. The computer-aided holophotoelastic method. *Experimental Mechanics*, 30(2):135–144, 1990.

[17] M Solaguren-Beascoa Fernández, JM Alegre Calderón, PM Bravo Díez, and II Cuesta Segura. Stress-separation techniques in photoelasticity: a review. *The Journal of Strain Analysis for Engineering Design*, 45(1):1–17, 2010.

[18] ME Fourney. Application of holography to photoelasticity. *Experimental mechanics*, 8(1):33–38, 1968.

[19] Cesar A Sciammarella. The moiré method—a review. *Experimental Mechanics*, 22(11):418–433, 1982.

[20] Gianni Nicoletto. Moiré interferometry determination of residual stresses in the presence of gradients. *Experimental Mechanics*, 31(3):252–256, 1991.

[21] A McDonach, J McKelvie, P MacKenzie, and CA Walker. Improved moiré interferometry and applications in fracture mechanics, residual stress and damaged composites. *Experimental Techniques*, 7(6):20–24, 1983.

[22] Judy D Wood, Rizhi Wang, Steve Weiner, and David H Pashley. Mapping of tooth deformation caused by moisture change using moire interferometry. *Dental Materials*, 19(3):159–166, 2003.

[23] D Post and WA Baracat. High-sensitivity moiré interferometry—a simplified approach. *Experimental Mechanics*, 21(3):100–104, 1981.

[24] MA Sutton, WJ Wolters, WH Peters, WF Ranson, and SR McNeill. Determination of displacements using an improved digital correlation method. *Image and vision computing*, 1(3):133–139, 1983.

[25] MA Sutton, Cheng Mingqi, WH Peters, YJ Chao, and SR McNeill. Application of an optimized digital correlation method to planar deformation analysis. *Image and Vision Computing*, 4(3):143–150, 1986.

[26] Carl D Meinhart, Steve T Wereley, and Juan G Santiago. Piv measurements of a microchannel flow. *Experiments in fluids*, 27(5):414–419, 1999.

[27] Richard D Keane and Ronald J Adrian. Theory of cross-correlation analysis of piv images. *Applied scientific research*, 49(3):191–215, 1992.

[28] Fulvio Scarano. Iterative image deformation methods in piv. *Measurement science and technology*, 13(1):R1, 2002.

[29] C Franck, S Hong, SA Maskarinec, DA Tirrell, and G Ravichandran. Three-dimensional full-field measurements of large deformations in soft materials using confocal microscopy and digital volume correlation. *Experimental Mechanics*, 47(3):427–438, 2007.

[30] Thomas A Berfield, Jay K Patel, Robert G Shimmin, Paul V Braun, John Lambros, and Nancy R Sottos. Fluorescent image correlation for nanoscale deformation measurements. *Small*, 2(5):631–635, 2006.

[31] G Vendroux and WG Knauss. Submicron deformation field measurements: Part 2. improved digital image correlation. *Experimental Mechanics*, 38(2):86–92, 1998.

[32] Michael A Sutton, N Li, DC Joy, Anthony P Reynolds, and Xiaodong Li. Scanning electron microscopy for quantitative small and large deformation measurements part i: Sem imaging at magnifications from 200 to 10,000. *Experimental mechanics*, 47(6):775–787, 2007.

[33] J Kang, M Jain, DS Wilkinson, and JD Embury. Microscopic strain mapping using scanning electron microscopy topography image correlation at large strain. *The Journal of Strain Analysis for Engineering Design*, 40(6):559–570, 2005.

[34] Zhi-Feng Zhang, Yi-Lan Kang, Huai-Wen Wang, Qing-Hua Qin, Yu Qiu, and Xiao-Qi Li. A novel coarse-fine search scheme for digital image correlation method. *Measurement*, 39(8):710–718, 2006.

[35] Peng Zhou and Kenneth E Goodson. Subpixel displacement and deformation gradient measurement using digital image/speckle correlation (disc). *Optical Engineering*, 40(8):1613–1620, 2001.

[36] PF Luo, YJ Chao, MA Sutton, and WH Peters Iii. Accurate measurement of three-dimensional deformations in deformable and rigid bodies using computer vision. *Experimental Mechanics*, 33(2):123–132, 1993.

[37] B Pan, H Xie, L Yang, and Z Wang. Accurate measurement of satellite antenna surface using 3d digital image correlation technique. *Strain*, 45(2):194–200, 2009.

[38] MA Sutton, X Ke, SM Lessner, M Goldbach, M Yost, F Zhao, and HW Schreier. Strain field measurements on mouse carotid arteries using microscopic three-dimensional digital image correlation. *Journal of Biomedical Materials Research Part A*, 84(1):178–190, 2008.

[39] PF Luo and SS Liou. Measurement of curved surface by stereo vision and error analysis. *Optics and lasers in engineering*, 30(6):471–486, 1998.

[40] Brian K Bay, Tait S Smith, David P Fyhrie, and Malik Saad. Digital volume correlation: three-dimensional strain mapping using x-ray tomography. *Experimental mechanics*, 39(3):217–226, 1999.

[41] BK Bay. Methods and applications of digital volume correlation. *The Journal of Strain Analysis for Engineering Design*, 43(8):745–760, 2008.

[42] Tait S Smith, Brian K Bay, and Mark M Rashid. Digital volume correlation including rotational degrees of freedom during minimization. *Experimental Mechanics*, 42(3):272–278, 2002.

[43] Carmel Majidi. Soft robotics: a perspective—current trends and prospects for the future. *Soft Robotics*, 1(1):5–11, 2014.

[44] Ig Mo Koo, Kwangmok Jung, Ja Choon Koo, Jae-Do Nam, Young Kwan Lee, and Hyouk Ryeol Choi. Development of soft-actuator-based wearable tactile display. *Robotics, IEEE Transactions on*, 24(3):549–558, 2008.

[45] Kytai Truong Nguyen and Jennifer L West. Photopolymerizable hydrogels for tissue engineering applications. *Biomaterials*, 23(22):4307–4314, 2002.

[46] Allan S Hoffman. Hydrogels for biomedical applications. *Advanced drug delivery reviews*, 64:18–23, 2012.

[47] Venkat R Krishnan, Chung Yuen Hui, and Rong Long. Finite strain crack tip fields in soft incompressible elastic solids. *Langmuir*, 24(24):14245–14253, 2008.

[48] Micah Dembo and Yu-Li Wang. Stresses at the cell-to-substrate interface during locomotion of fibroblasts. *Biophysical journal*, 76(4):2307–2316, 1999.

[49] Wesley R Legant, Jordan S Miller, Brandon L Blakely, Daniel M Cohen, Guy M Genin, and Christopher S Chen. Measurement of mechanical tractions exerted by cells in three-dimensional matrices. *Nature methods*, 7(12):969–971, 2010.

[50] Stacey A Maskarinec, Christian Franck, David A Tirrell, and Guruswami Ravichandran. Quantifying cellular traction forces in three dimensions. *Proceedings of the National Academy of Sciences*, 106(52):22108–22113, 2009.

[51] Ariel Livne, Eran Bouchbinder, Ilya Svetlizky, and Jay Fineberg. The near-tip fields of fast cracks. *Science*, 327(5971):1359–1363, 2010.

[52] Li Liu and Elise F Morgan. Accuracy and precision of digital volume correlation in quantifying displacements and strains in trabecular bone. *Journal of biomechanics*, 40(15):3516–3520, 2007.

[53] Matthew S Hall, Rong Long, Chung-Yuen Hui, and Mingming Wu. Mapping three-dimensional stress and strain fields within a soft hydrogel using a fluorescence microscope. *Biophysical journal*, 102(10):2241–2250, 2012.

[54] Ted Belytschko, Yun Yun Lu, and Lei Gu. Element-free galerkin methods. *International journal for numerical methods in engineering*, 37(2):229–256, 1994.

[55] Peter Lancaster and Kes Salkauskas. Surfaces generated by moving least squares methods. *Mathematics of computation*, 37(155):141–158, 1981.

[56] Dermot H McLain. Drawing contours from arbitrary data points. *The Computer Journal*, 17(4):318–324, 1974.

[57] MGD Geers, R De Borst, and WAM Brekelmans. Computing strain fields from discrete displacement fields in 2d-solids. *International Journal of Solids and Structures*, 33(29):4293–4307, 1996.

[58] LRG Treloar. The elasticity of a network of long-chain molecules. i. *Rubber Chemistry and Technology*, 16(4):746–751, 1943.

[59] LRG Treloar. The elasticity of a network of long-chain molecules—ii. *Trans. Faraday Soc.*, 39:241–246, 1943.

[60] Nicola Bonora and Eric Brown. *Numerical Modeling of Materials Under Extreme Conditions*, volume 35. Springer, 2014.

[61] Gerhard A Holzapfel. Nonlinear solid mechanics: a continuum approach for engineering science. *Meccanica*, 37(4):489–490, 2002.

[62] TH Lengyel, Rong Long, and P Schiavone. Effect of interfacial slippage on the near-tip fields of an interface crack between a soft elastomer and a rigid substrate. In *Proceedings of the Royal Society of London A: Mathematical, Physical and Engineering Sciences*, volume 470, page 20140497. The Royal Society, 2014.

[63] Gui-Rong Liu. *Meshfree methods: moving beyond the finite element method*. CRC press, 2010.

[64] Marc Duflot and Hung Nguyen-Dang. A meshless method with enriched weight functions for fatigue crack growth. *International Journal for Numerical Methods in Engineering*, 59(14):1945–1961, 2004.

[65] Mary C Boyce and Ellen M Arruda. Constitutive models of rubber elasticity: a review. *Rubber chemistry and technology*, 73(3):504–523, 2000.

[66] Cornelius T Leondes. *Structural Dynamic Systems Computational Techniques and Optimization: Computational Techniques*, volume 7. CRC Press, 1999.